npj | climate and atmospheric science

Article

Published in partnership with CECCR at King Abdulaziz University

https://doi.org/10.1038/s41612-025-01235-1

Divergent controls on surface and thermal offsets in permafrost across the three poles

Check for updates

Jia Liu[1,2], Dongliang Luo[1] ✉, Qingbai Wu[1], Wojciech Dobiński[3], Huijun Jin[4], Olga Makarieva[5], Fangfang Chen[1,2], Shizhen Li[1,2] & Raul-D. Șerban[6]

The thermal response of permafrost to climate change is quantified by two key metrics: the surface offset (*SO*), the mean annual temperature difference between near-surface air and the ground surface, and the thermal offset (*TO*), the equivalent difference between the ground surface and the top of permafrost. However, a comprehensive global synthesis of their magnitude, variability, and controlling drivers remains elusive. Here, synthesizing data from 117 sites across the three poles, we reveal a fundamental, scale-dependent decoupling of their controls. We show that *SO* is primarily controlled by large-scale climate, with precipitation dictating the similar large magnitude of *SO* in the Arctic (3.1 ± 0.3 °C, cold-humid permafrost) and the Third Pole (3.2 ± 0.2 °C, warm-dry permafrost), but small in Antarctica (1.0 ± 0.2 °C, ultraxerous permafrost). In contrast, *TO* is predominantly determined by local-scale substrate properties, being markedly negative in the Arctic (−0.5 ± 0.2 °C), weakly negative in the Third Pole (−0.2 ± 0.1 °C), and negligible in Antarctica (−0.1 ± 0.1 °C). Critically, this substrate control can be overridden by regional climate, such as advective heat transport following rainfall. This synthesis establishes the first global benchmarks for permafrost thermal states and reveals a paradigm of divergent, multi-scale controls essential for improving models that predict the fate of Earth's thawing cryosphere.

Permafrost, ground (soil or rock, including ice and organic materials) remaining at or below 0 °C for at least two consecutive years[1,2], underlies approximately 16% of Earth's exposed land surface and a quarter of the Northern Hemisphere[3]. In recent decades, accelerated warming and intensified anthropogenic activity, particularly within Arctic and high-mountain environments, have driven widespread permafrost degradation, which is manifested by rising ground temperatures, deepening active layers, the formation of *taliks*, and the disappearance of sporadic or isolated permafrost[4–9]. The consequences of permafrost thaw are profound, threatening local-to-global systems by releasing vast quantities of greenhouse gases[10–12], triggering abrupt landscape changes[13–15], altering hydrological and ecological regimes[16,17], and damaging critical infrastructure[18,19]. Mitigating these impacts requires a predictive understanding of the permafrost thermal regime, which depends on the complex interplay between atmospheric conditions, surface characteristics, and subsurface heat transfer[20].

A precise characterization of the permafrost thermal state hinges on distinguishing among key near-surface temperatures: (1) the near-surface air temperature (*Ta*), typically measured at a screen height of 2.0 m above the ground surface; (2) the land-surface temperature (*LST*) measured on the canopy surface (including bare ground or bed rocks, vegetation canopy in summer, and snow surface in winter); and (3) the ground surface temperature (*GST*) measured at 0–5 cm depth just beneath the surface cover[21]. Of these, *GST* is the most critical as it directly governs ground thermal dynamics and serves as the upper boundary condition for subsurface heat-flow models. While *Ta* is a primary climatic driver in permafrost models[22–24], its influence is modulated by the surface characteristics. Similarly, *LST*, increasingly available via remote sensing, is not a direct proxy for *GST*, and converting between them requires detailed, site-specific information that is often unavailable.

Systematic differences between the mean annual values of these temperatures give rise to two critical phenomena: the surface offset (*SO*) and

---

[1]State Key Laboratory of Cryospheric Science and Frozen Soil Engineering, Northwest Institute of Eco-Environment and Resources, Chinese Academy of Sciences, Lanzhou, China. [2]University of Chinese Academy of Sciences, Beijing, China. [3]Faculty of Natural Sciences, University of Silesia in Katowice, Institute of Earth Sciences, Sosnowiec, Poland. [4]School of Ecology, Northeast Forestry University, Harbin, China. [5]Melnikov Permafrost Institute, Yakutsk, Russia. [6]Faculty of Agricultural, Environmental and Food Sciences, Free University of Bozen-Bolzano, Bolzano, Italy. ✉e-mail: luodongliang@lzb.ac.cn

thermal offset (*TO*). These offsets are fundamental for understanding permafrost-climate relationships and for accurately modelling permafrost distribution and evolution[20,25,26]. Conceptually, the *SO* bridges the gap from mean annual near-surface air temperature (*MAAT*), or the mean annual land-surface temperature (*MAST*), to the mean annual ground surface temperature (*MAGST*) in two steps: from near-surface air to the land surface, and from the land surface to the ground surface. In practice, however, the *SO* is calculated as a single, integrated metric: $SO = MAGST - MAAT$[27,28].

The *SO* arises because the ground surface is decoupled from atmospheric temperature extremes by an array of moderating factors, such as snow cover insulation in winter and evaporative cooling or vegetation shading in summer[20,25]. Consequently, the spatial variability of the *SO* is fundamentally controlled by the surface energy balance, which is strongly influenced by site-specific characteristics, including vegetation, snowpack properties, organic layer thickness, soil moisture, surface water, hydrological processes, and microtopography[29]. To parameterize this complex relationship in models, the *N*-factor, the ratio of ground surface to air thawing/freezing indices, is commonly used. This factor provides a practical tool for linking *MAAT* and *MAGST* by capturing how surface characteristics modulate thermal energy transfer in permafrost regions.

The *TO*, originally described by Burn and Smith[30] and Romanovsky and Osterkamp[31], represents the phenomenon where the temperature at the top of the permafrost (*TTOP*) is typically lower than *MAGST* ($TO = TTOP - MAGST$)[32]. This offset is primarily caused by the pronounced difference between the thermal conductivity of frozen (K_f) and thawed (K_t) soils in the active layer. Because K_f typically exceeds K_t, particularly in moist soils where ice is more conductive than water[31], heat is conducted away from the permafrost table more efficiently in winter than it is conducted toward it in summer. This asymmetry results in a net cooling effect at the bottom of the active layer and thus at the permafrost table itself[33,34]. However, this equilibrium-based explanation is insufficient under modern climate change. Under such disequilibrium conditions, the observed *TO* also reflects transient thermal lags, complicating the direct inference of permafrost presence from *MAGST* alone. The magnitude of the *TO* is therefore highly variable, depending on soil-moisture content, ground-ice content, organic content, and the overall thermal regime. This leads to distinct *TO* values in different permafrost environments, ranging from cold-humid (ice-rich and cold) permafrost[31,35] to warm, ice-rich permafrost; and from ultraxerous (ice-poor but cold) permafrost[35,36] to warm and relatively dry permafrost[25,37,38]. These types manifest differently across the three poles: for instance, the cold-humid type is widespread in Arctic tundra lowlands, while warm, ice-rich permafrost is common in sub-Arctic regions. The ultraxerous permafrost in the surrounding Antarctica is cold but with limited ground-ice content, while the warm-dry permafrost in the Third Pole has relatively high temperature and less ground ice content[25,35,39,40].

Despite the recognized importance of the *SO* and *TO*, a comprehensive, cross-polar synthesis assessing the universality of their drivers remains elusive. Research has often been confined to specific regions or permafrost types, leaving a critical knowledge gap: it is unknown whether the established drivers operate uniformly across disparate climate envelopes or if their relative importance shifts under the non-equilibrium conditions of rapid warming. This uncertainty fundamentally limits our ability to build robust, globally applicable permafrost models. Here, we address this gap by presenting the first comprehensive, data-driven assessment of *SO* and *TO* across the Arctic, Antarctica, and the Third Pole. Specifically, our aims are to: (1) establish a global baseline for *SO* and *TO* variability across these contrasting polar environments; (2) quantify and compare the relative importance of key environmental drivers, identifying both common principles and critical regional differences that may challenge existing paradigms; and (3) use these findings to highlight the limitations of current equilibrium-based assumptions and inform the development of next-generation permafrost models.

Results and discussion

A global baseline reveals contrasting polar offsets

The *SO* is highly heterogeneous across the selected Arctic and sub-Arctic permafrost sites, ranging from −0.5 to 8.4 °C with a mean of 3.1 ± 0.3 °C ($CV = 0.7$) (Figs. 1 and 3). While the warm-dry permafrost of the Third Pole

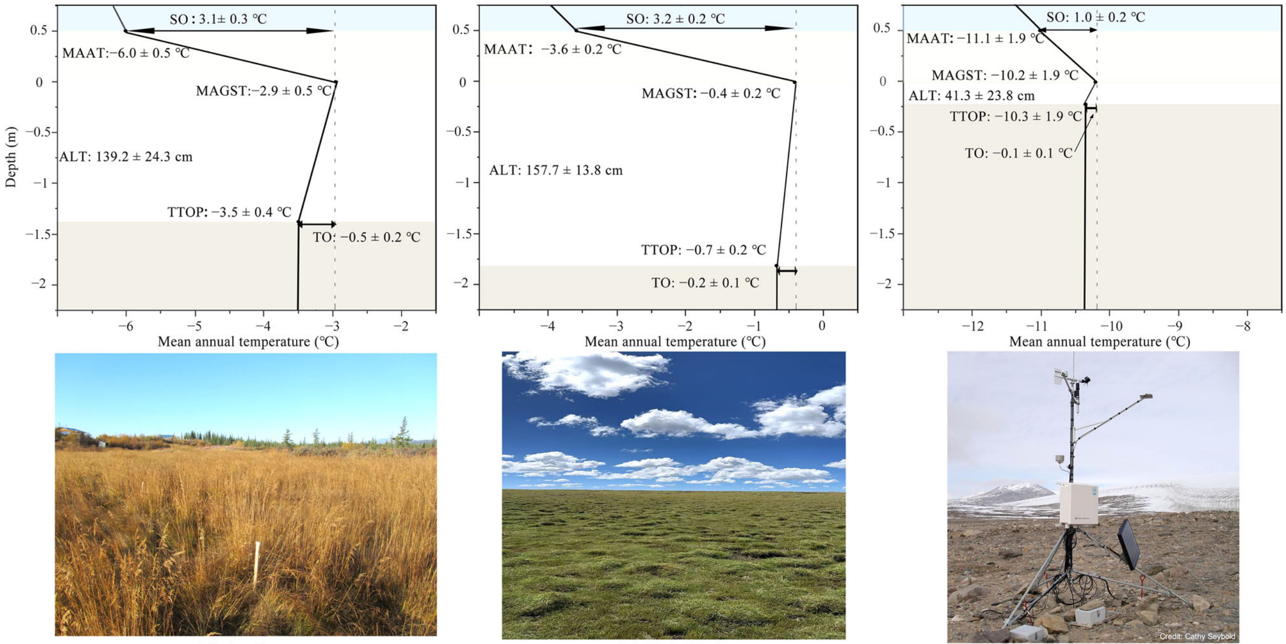

(a) Arctic (b) Third Pole (c) Antarctica

Fig. 1 | Permafrost thermal state profiles across the three poles. This figure presents the permafrost thermal state profiles (numbers represent the mean ± standard error), with example sites shown: (**a**) Arctic (e.g. Arctic Village site, Forest tundra); (**b**) Third Pole (e.g. CLP site, Grassland); and (**c**) Antarctica (e.g. Scott Base site, No vegetation). *ALT*, *MAAT*, *MAGST*, *TTOP*, *SO*, and *TO* denote active layer thickness, mean annual air temperature, mean annual ground surface temperature, mean annual temperature at the top of permafrost, surface offset, and thermal offset, respectively. The photograph in (**a**) is courtesy of the Global Terrestrial Network for Permafrost (GTN-P). The photograph in panel (**b**) was taken by the authors. The photograph in panel (**c**) is provided by the USDA Natural Resources Conservation Service and is credited to Cathy Seybold.

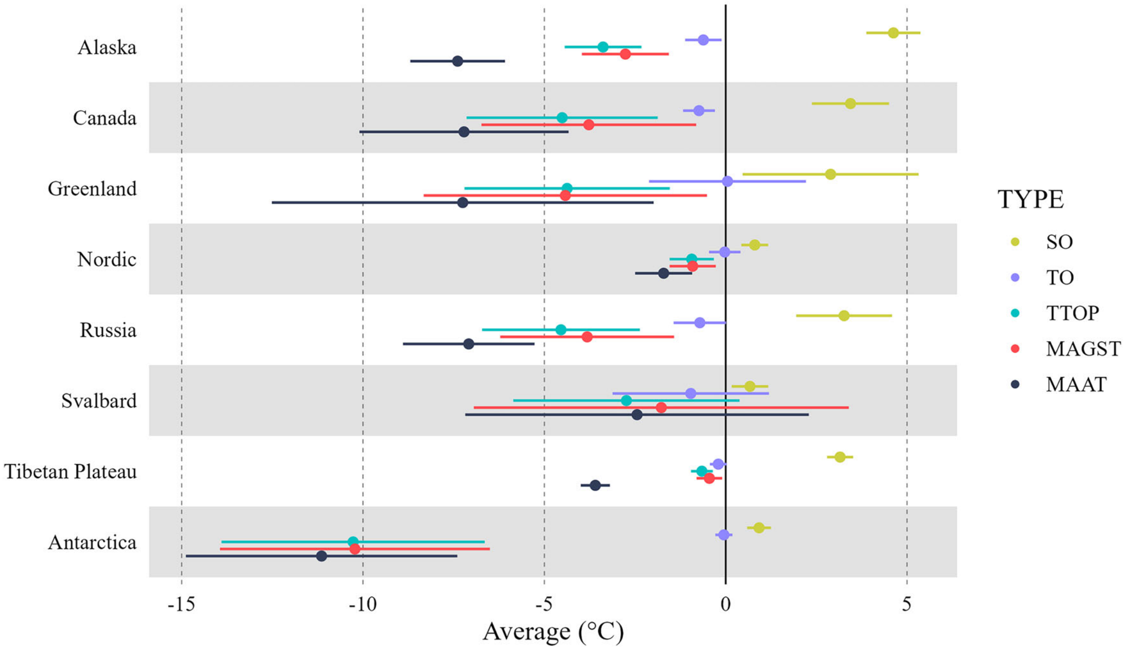

Fig. 2 | Surface offset (*SO*), thermal offset (*TO*), mean annual temperature at the top of permafrost (*TTOP*), mean annual ground surface temperature (*MAGST*), and mean annual air temperature (*MAAT*) in different permafrost regions across the Earth. The forest plot shows the mean (dot) and 95% confidence interval (horizontal line) for each sub-region.

exhibits a similar mean *SO* of 3.2 ± 0.2 °C but with markedly lower spatial variability (*CV* = 0.3). The distinct pattern of *SO* differs considerably from those typically found in high-latitude Arctic environments[41], and it likely reflects the Third Pole's mid-latitude setting and consistent dwarf vegetation or even bare ground, which lacks the high latitudes' extreme seasonal contrasts in daylight and annual air temperature range. Antarctica's ultraxerous permafrost presents a third distinct regime; the combination of the lowest *MAAT* (−11.1 ± 1.9 °C) and *MAGST* (−10.2 ± 1.9 °C) results in a much smaller mean *SO* of 0.9 ± 0.2 °C, which is nonetheless the most variable relative to its mean (*CV* = 0.8) (Figs. 1 and 2).

These pan-polar patterns are further modulated by regional climate and landscape characteristics. For example, high *SO* is characteristic of forested areas of Alaska and Canada compared to the high Arctic tundra of Greenland or Svalbard (Fig. 2). The highest regional mean *SO* in cold-humid Arctic permafrost regions were observed in Alaska (4.6 °C), likely driven by strong surface insulation from thick winter snowpacks and dense vegetation, which create a significant contrast between a low *MAAT* of −7.1 °C and a considerably higher *MAGST* of −2.8 °C. Conversely, small *SO* is characteristic of maritime climates, such as those in Iceland, Norway, and Svalbard, where *MAAT* and *MAGST* are more closely coupled. It is important to note that while Antarctica exhibits the lowest mean temperatures, similarly cold and even colder thermal regimes exist in non-Antarctic regions, particularly at high elevations and in the high-latitude continental interiors of the Arctic.

The *TO* demonstrates even more pronounced divergence among the three poles. The cold-humid Arctic is characterized by a predominantly negative mean *TO* of −0.5 ± 0.2 °C (ranging from −4.2 to 2.4 °C) and high variability (*CV* = 2.3), with the most negative values (−0.6 °C to −1.0 °C) concentrated in continental North America, Russia, and Svalbard sites (Figs. 2 and 4). This classic negative offset, however, is absent in the other polar regions. Sites in Greenland and the Nordic region show mean values clustering near zero. While the warm-dry Third Pole exhibits a mean *TO* near zero (−0.2 ± 0.1 °C), this represents a reversal of the typically negative *TO* found in many Arctic regions. The *TO* range is also much narrower, from −1.5 °C to 2.0 °C, than in the Arctic. Notably, 72% of the study sites in the Third Pole exhibit positive *TO*, representing a reversal of the classic *TO* signal, which is a phenomenon consistent with observations from the cold, dry (ultraxerous) permafrost of East Antarctica[42]. Despite a slightly positive mean *TO* of 0.1 ± 0.1 °C, Antarctica exhibits the highest spatial heterogeneity of *TO* (*CV* = 8.0). This extreme variability is closely linked to the continent's prevailing conditions of low air temperature (−11.1 ± 1.9 °C), thin snow depth (0.03 ± 0.02 m), and negligible soil moisture (0.13 ± 0.03 m^3/m^3). Collectively, this tri-polar grouping, from the strong negative *TO* in the continental Arctic to the near-zero or positive values in the Third Pole and Antarctica, powerfully underscores the sensitivity of subsurface heat transfer to both large-scale climate and local substrate properties[34].

Surface offset is governed by large-scale climate forcing

SO is independent of permafrost presence, although the ground thermal regime influenced by permafrost can affect *SO*, which is strongly mediated by surface characteristics that control the energy exchange between the atmosphere and the ground[25,36,43,44]. To untangle the hierarchy of controls on the *SO*, we employed a machine learning approach quantified by SHAP values. Our analysis reveals that total annual precipitation is the overwhelmingly dominant global driver of *SO* (mean absolute SHAP = 0.81), highlighting the primary role of large-scale water input in setting the ground's thermal state (Fig. 5). Geographic location, evaporation, and vegetation density serve as significant, albeit secondary, predictors.

While large-scale climate sets the baseline, local surface characteristics, most notably vegetation cover and snow regimes, ultimately modulate the magnitude of the *SO* by controlling the surface energy balance[20,25]. This results in a thermal decoupling between the atmosphere and the ground surface, a process strongly amplified by local conditions. In the Arctic, this heterogeneity is driven by the complex interplay of vegetation, snow, and soil properties. For example, ecosystems like coniferous forests generally enhance summer shading and trap insulating snow, which keeps the ground warmer than the near-surface air on an annual basis[45]. These responses are not unique to specific regions, as similar *SO* magnitudes have been reported in parts of the western Canadian Arctic[46,47]. In contrast, ecosystems with low-stature or sparse vegetation like tundra or polar deserts often display small or even negative *SO* (e.g., −0.1 °C at Chukochya River site, Russia)

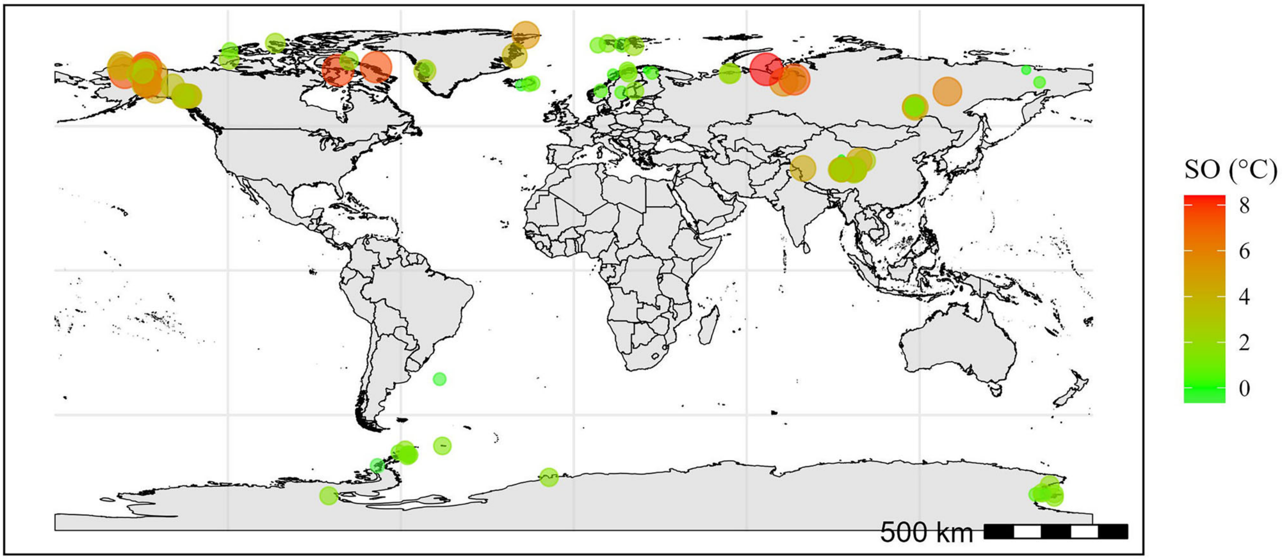

Fig. 3 | Spatial variability of surface offset (*SO*) in permafrost regions across the three poles. Each point represents a monitoring site of permafrost thermal state (see Fig. 8 for locations) in the Arctic, Antarctica, and the Third Pole. Point color indicates the *SO* (°C). Point transparency is used to reduce visual overlap in areas with high site density. The map uses a Plate Carrée projection.

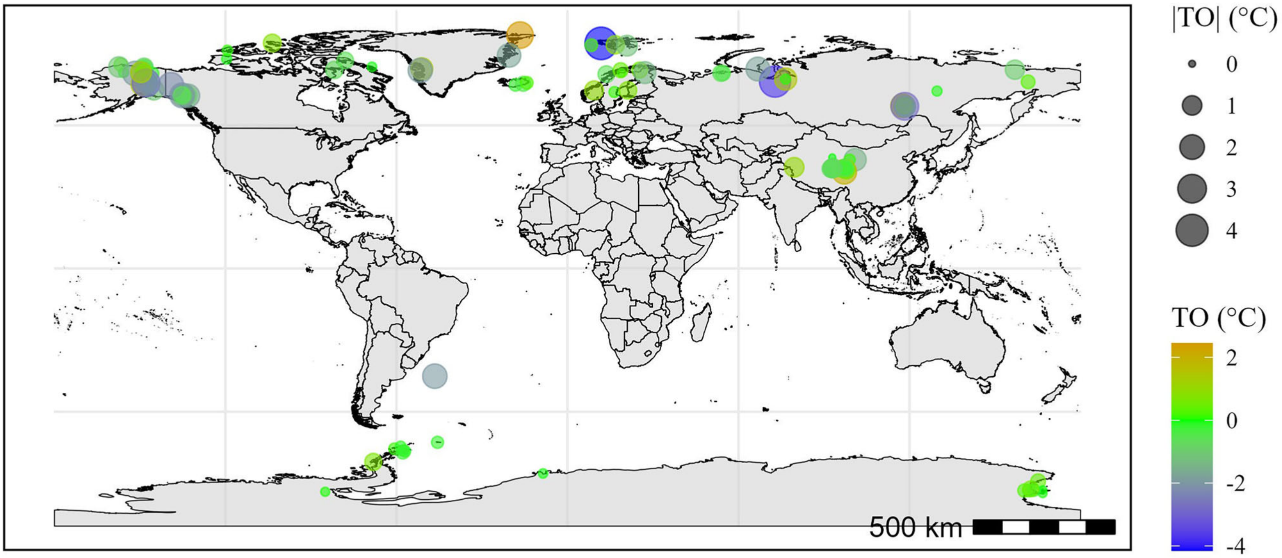

Fig. 4 | Spatial variability of thermal offset (*TO*) in permafrost regions across the three poles. Each point represents a permafrost thermal state monitoring site, corresponding to locations presented in Fig. 8 and distributed across the Arctic, Antarctica, and the Third Pole. Point color indicates the *TO* (°C), revealing the direction of the offset: positive values signify that the permafrost top is warmer than the ground surface on average, while near-zero and negative values indicate it is colder. Simultaneously, point size corresponds to the absolute magnitude, |*TO*|, thereby illustrating the intensity of the subsurface thermal gradient deviation from a simple conductive regime. Point transparency is used to reduce visual overlap in areas with high site density. The map uses a Plate Carrée projection.

(Fig. 3), primarily driven by efficient radiative cooling and the reduced insulating effect of wind-redistributed snow. Furthermore, the insulating capacity of the snowpack is highly dependent on its physical structure; the light, low-density snow characteristic of the Arctic provides more effective insulation than the denser, more compacted snowpack often found in boreal regions. The ecosystems like forest-tundra also show smaller *SO* (e.g., 0.4 °C at Kevo (Valsjeaggl 1) site, Nordic region), particularly in deciduous stands where canopy loss after leaf fall reduces snow interception and winter insulation, while summer evapotranspirative cooling can also lower ground surface temperatures. Moreover, soil moisture and water table levels affect ground temperatures, with warmer conditions typically observed in drier soils and cooler temperatures in wetter soils due to differences in thermal conductivity. This thermal effect of soil moisture is less pronounced in conifer-dominated stands, where canopy structure is largely retained through winter.

In the Third Pole, vegetation is a primary local factor influencing the thermal regime of the ground surface. The magnitude of *SO* is a function of vegetation structure (cover density and height), which modulates the surface energy balance[48]. Despite the often-uniform appearance of sparse dwarf vegetation, the effect of vegetation on *SO* is complex and varies with microenvironment. For instance, the *SO* in sparse alpine steppe (e.g., 3.1 °C at ELH site) is notably higher than in alpine swamp meadow (e.g., 2.2 °C at CLP2 site) (Fig. 3). Similarly, grassland-covered sites have a larger *SO* (3.2 °C) compared to sparsely vegetated dwarfk surfaces (*SO* = 2.9 °C) or bare ground sites (*SO* = 2.5 °C). A key feature distinguishing the Third Pole from the Arctic, however, is the diminished insulating role of its typically

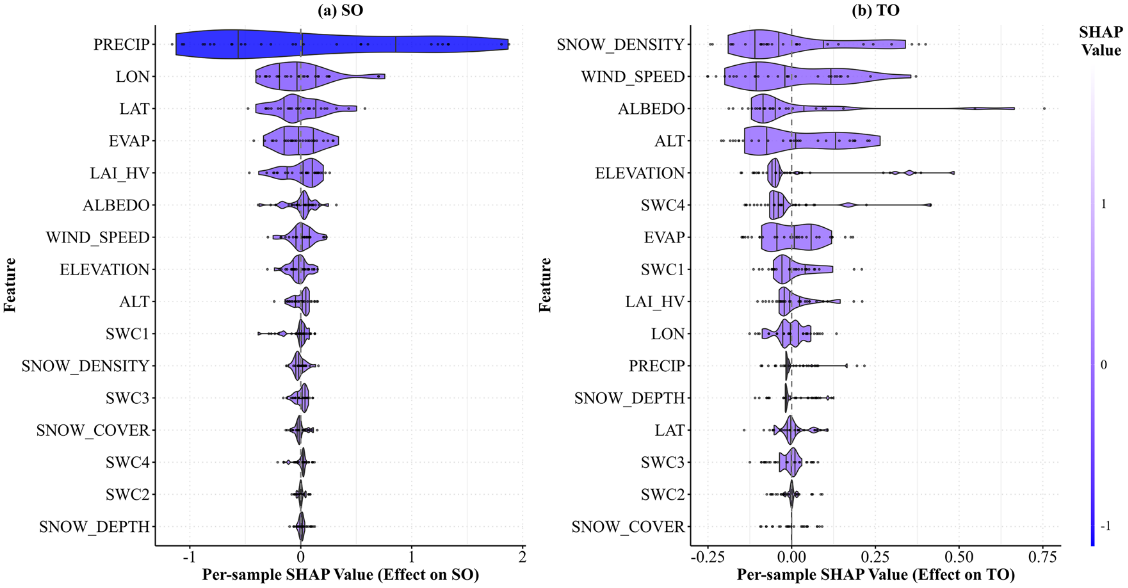

Fig. 5 | Influence of environmental drivers on the thermal offset (*TO*) and surface offset (*SO*), quantified using SHAP values. The violin plots show the distribution of SHAP values for the primary drivers influencing (**a**) the *TO* and (**b**) the *SO*. Each point represents a single observation; its position on the *x*-axis is its SHAP value, indicating the direction and magnitude of that driver's contribution to the model prediction. The violin shape visualizes the probability density of SHAP values for each driver, with vertical dashed lines marking the 25th, 50th (median), and 75th percentiles. The drivers (features) are ranked vertically by their global importance, calculated as the mean absolute SHAP value across all observations. The color of each point corresponds to the feature's value for that observation, with darker blue indicating lower feature values and lighter purple/white indicating higher values, as shown in the color bar. Feature abbreviations are as follows: SNOW_DENSITY, annual snow density; WIND_SPEED, 10 m annual wind speed; ALBEDO, annual surface albedo; ALT, active layer thickness; ELEVATION, site elevation; SWC1-4, annual volumetric soil water content at different depths (1: 0–10 cm, 2: 10–40 cm, 3: 40–100 cm, 4: 100–200 cm); EVAP annual evaporation from vegetation transpiration, LAI_HV annual leaf area index of high vegetation, LON site longitude, LAT site latitude, PRECIP total annual precipitation, SNOW_DEPTH annual snow depth, SNOW_COVER annual snow cover fraction.

thin and ephemeral snow cover, a result of strong winds and high solar radiation promoting sublimation[49]. This, in turn, reduced snow influence amplifies the importance of other subsurface processes, particularly seasonal freeze-thaw cycles. In the region's widespread discontinuous and sporadic permafrost, where ground temperatures are close to 0 °C, these phase transitions involve substantial latent heat exchange. This process effectively buffers ground temperature fluctuations and thus strongly influences the *SO* magnitude. The strength of this buffering, in turn, depends on active layer thickness, substrate type, and ice content[50,51]. The spatial variability of this latent heat buffering, therefore, helps explain the large-scale patterns observed in *SO*. For example, lower *SO* (e.g., 1.3 °C at CLP3 site, 1.2 °C at ZLH1 site) is observed in the discontinuous permafrost of the Heihe and Yellow River source areas. In contrast, significantly larger *SO* (≥3.0 °C) is found in the colder, continuous permafrost of the Yangtze River source area (e.g., 5.8 °C at the Kunlun Basin site, 4.4 °C at TSH site) (Fig. 4).

In Antarctica, the *SO* is generally small, and its magnitude is strongly linked to the ambient thermal regime. For instance, extremely cold interior sites like Mt. Fleming and Victoria Valley 1 sites (near −23.0 °C) show minimal *SO* of 0.5 °C and 0.3 °C, respectively, while peripheral maritime environments like Limnopolar Lake site (1.6 °C) exhibit relatively larger *SO*. The small mean *SO* in the Antarctica is attributed to its unique seasonal thermal dynamics. During the austral summer, high insolation and thin snow cover allow the ground surface temperature to warm well above air temperature, creating a positive *SO*. Conversely, during the wintertime, a thin or non-existent snowpack provides minimal insulation, facilitating strong ground surface cooling. This can lead to a negative *SO* at some sites, including Bull Pass, MarblePoint, and Rothera, where the ground surface becomes colder than the overlying near-surface air. This winter cooling is intensified by a thin or absent snowpack, offering negligible thermal insulation due to strong winds and sublimation, a condition paralleling the limited insulating capacity on the Third Pole. The snowpack's persistence is itself constrained by strong winds driving sublimation and high solar radiation promoting melt, often rendering winter-spring accumulation ephemeral[44]. The influence of vegetation on the ground thermal regime is minimal due to its extreme sparsity, with mosses and lichens covering < 5% of the ice-free ground surface[52]. This lack of plant cover prevents significant snow trapping and results in minimal thermal differences between land covers, as evidenced by the similar *SO* at Granite Harbour site (bare ground, 1.6 °C) and Low Head site (tundra, 1.6 °C). The absence of vegetation also means the ground moisture balance is almost entirely governed by ice and snowmelt dynamics. Therefore, this minimal biophysical regulation makes Antarctica a unique environment for studying abiotic controls on permafrost thermal states[53].

A particularly striking result is the low predictive power of traditionally emphasized snow variables. This finding is counterintuitive, given that snow cover is considered a primary driver of *SO* differentiation in polar environments due to its insulating properties[34,54,55]. Conceptually, the thermal effect of snow on the *SO* is often quantified through the 'nival offset', which models how snow's insulation modifies the surface freezing index[20]. However, this approach requires detailed parameters that are often unavailable at a global scale. Furthermore, our machine learning results suggest the snow-*SO* relationship is more complex and context-dependent than captured by a single index. To investigate this complexity, we conducted a targeted meta-analysis of the statistical relationship between key snow variables (snow depth, snow cover, and snow density) and *SO* across distinct biomes (Fig. 5a).

This synthesis reveals that the net effect of snow on *SO* is consistently negative in vegetated terrains, a relationship that is spatially variable and dependent on vegetation type. The effect was significant in both the vegetated Arctic (slope = −0.59, 95% CI: −1.04 to −0.15) and the Third Pole's grasslands (slope = −0.45, 95% CI: −0.64 to −0.27) (Fig. 6). This pervasive negative correlation, where denser snow leads to a lower *SO*, indicates that snow's direct insulating effect is often outweighed by a suite of interacting biogeophysical processes, such as summer shading from vegetation, altered

Fig. 6 | Forest plot from the meta-analysis examining the relationship between snow variables and the surface offset (*SO*), with results grouped by vegetation type and polar region. The total sample size displayed in the forest plot represents only the samples from region-vegetation type combinations where a valid regression of snow-related variables (snow depth, density, and cover) on *SO* could be performed, excluding samples with missing data or insufficient variation within their group. Grey squares indicate the effect size (slope) from individual studies, with horizontal lines representing the 95% confidence intervals (CI). The size of each square is proportional to that study's weight in the meta-analysis. The blue diamond shows the pooled summary effect and 95% CI for each vegetation-region subgroup and the overall meta-analysis. The vertical dashed line at zero represents the line of no effect. The red horizontal bar shows the 95% prediction interval for the overall summary effect. Heterogeneity statistics (I^2 and p-value) are provided for each subgroup.

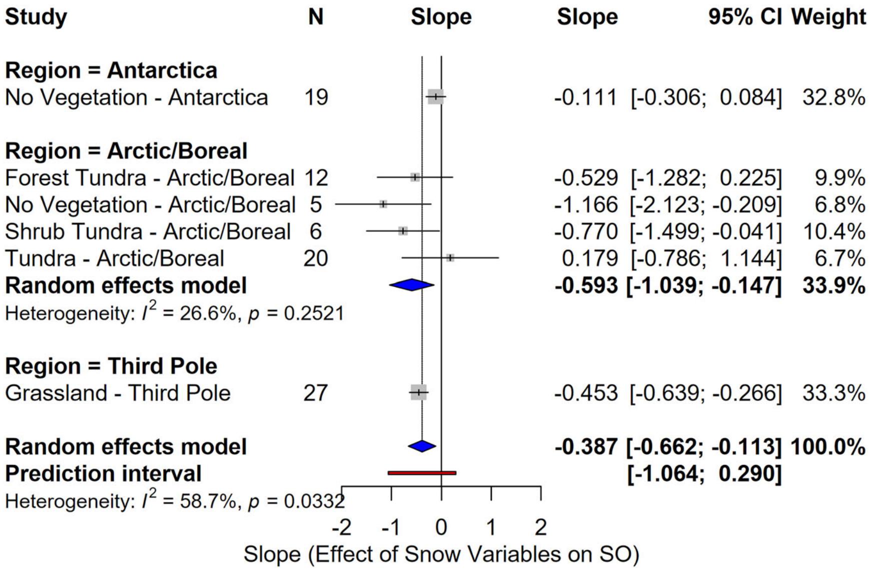

melt dynamics, and modified subsurface thermal properties[6,56,57]. In contrast, non-vegetated terrains exhibit a different dynamic. While the relationship in Antarctica was non-significant, the non-vegetated Arctic showed a strong, significant negative effect (slope = −1.17, 95% CI: −2.12 to −0.21), notably stronger than in its vegetated counterpart. This suggests that in the absence of complex buffering from vegetation, the thermal effect of snow reverts to a more direct insulating role.

Our dual-scale analysis thus reveals that while large-scale precipitation governs the overall *SO*, its final magnitude is finely tuned by the context-specific interactions between snow and local surface characteristics. This interplay drives substantial regional variability, reflecting critical differences in vegetation, such as shrub height in tundra areas and the contrasting thermal effects across treeline boundaries[58]. Fundamentally, these multi-faceted biogeophysical processes observed in vegetated terrain, where surface heterogeneity can amplify complex feedbacks between the atmosphere and ground thermal regime[54,59], contrast with the more direct insulating role of snow on non-vegetated surfaces. The resulting complexity presents a significant challenge for modeling permafrost thermal regimes, as subsurface conditions, particularly latent heat effects during freeze-thaw cycles, also significantly influence how snow cover affects *MAGST*[50,51]. Therefore, improving projections of permafrost thermal response to environmental change will require integrated approaches that explicitly account for the coupled dynamics of snow distribution, vegetation, and subsurface thermal and hydrological properties[54].

Thermal offset is fine-tuned by local substrate properties

The magnitude and sign of the *TO* are governed by the asymmetry of heat conduction during seasonal freeze-thaw cycles, a process primarily controlled by the ratio of thawed to frozen thermal conductivity ($r_k = K_t/K_f$)[50]. A negative *TO* develops when frozen soil is more thermally conductive than thawed soil ($r_k < 1$), a condition typical for most organic-rich soils such as peat. Organic matter enhances water retention, leading to an ice-rich, highly conductive frozen state (e.g., with a K_t of 0.6 W/mK and a K_f of 1.2 W/mK, the resulting r_k is 0.5). This asymmetry causes winter heat loss through the frozen layer to be more efficient than summer heat gain through the less conductive thawed layer[31,34,60], resulting in a net cooling effect at depth and causing the *TTOP* to be lower than the *MAGST* (negative *TO*). Consequently, sites with thick organic layers typically yield large negative *TO*[61,62]. This pattern is geographically widespread, with examples from peat sites in Kashin_01k site, Russia (−0.5 °C), Tavvavuoma site, Nordic (−1.2 °C) region, and Nunk site, Greenland (−1.9 °C), and comparable *TO* magnitudes reported from peatlands in Canada[46,63].

Conversely, a minimal *TO* (near zero) occurs when thawed soil is comparably conductive to frozen soil ($r_k \approx 1$). This is characteristic of coarse-grained, well-drained materials like gravel, where low moisture content ensures that the thermal properties are dominated by the solid matrix[20,38], a condition exemplified by the Clyde River site in Canada (*TO* = −0.04 °C). However, this simple conductive framework is frequently modulated by other factors. Moisture-rich, fine-grained mineral soils (e.g., silts and clays) can exhibit $r_k < 1$ behavior similar to peat, while seasonal variations in soil moisture can alter or even reverse the expected offset[37]. Furthermore, non-conductive processes such as subsurface water flow can lead to positive *TO*, even in soil types where r_k typically favors a negative offset, as observed in Greenland (Fig. 2) and at the organic-rich Azarova-1 site in Russia (1.8 °C). The *ALT* further modifies heat transfer by amplifying the thermal conductivity contrast, as a deeper *ALT* allows the seasonal temperature signal to penetrate further and magnify the net effect. This may partially explain why deep *ALT* in the Nordic region (350.9 ± 114.4 cm) is associated with a larger *TO* magnitude, whereas the shallower mean *ALT* in Alaska (60.0 ± 5.3 cm) and parts of Russia (78.9 ± 11.4 cm) correspond to lower *TO*.

Our SHAP analysis identifies a clear hierarchy of controls for *TO*. Local physical factors dominate, led by snow density (SHAP = 0.14), wind speed (SHAP = 0.13), and albedo (SHAP = 0.12) (Fig. 5b). Notably, soil moisture at greater depths (100-200 cm) serves as an important secondary predictor (SHAP = 0.07), whereas the direct influence of large-scale precipitation is negligible (SHAP = 0.03). This dominance of local substrate and surface properties creates distinct regional thermal regimes.

The principle that the magnitude of *TO* is primarily governed by the ratio of thawed to frozen thermal conductivity within the active layer[20] explains the patterns observed in the Third Pole as well. Here, the prevalence of coarse-grained soils with limited organic matter and low moisture content results in comparable thermal conductivities between the frozen and thawed states, causing the r_k ratio to approach unity[25,37,38]. Consequently, in line with the governing theory, the *TO* in this region is characteristically small. In contrast to moisture-rich Arctic sites where a large negative *TO* enhances permafrost thermal stability[64], the smaller offset on the Third Pole provides less buffer against summer warming, contributing to a substantially thicker *ALT* (mean 157.7 ± 13.8 cm). Within this region, soil texture is a key control on spatial variability of *TO*. At 47% of sites dominated by sandy soils, the mean *TO* is small (−0.1 °C), but can become

Fig. 7 | Forest plot from the meta-analysis of the relationship between moisture and the thermal offset (*TO*), with results grouped by soil type and polar region. The total sample size shown in the forest plot includes only samples from groups defined by region and soil texture for which a valid regression of moisture variables (total precipitation and volumetric soil water at four depths) on *TO* could be performed, excluding those with missing data or insufficient variation. Grey squares indicate the effect size (slope) for individual studies, with horizontal lines representing the 95% confidence intervals (CI). The size of each square is proportional to that study's weight in the meta-analysis. The blue diamond represents the pooled summary effect and 95% CI for each soil-region subgroup and the overall analysis. The vertical dashed line at zero represents the line of no effect. The red horizontal bar shows the 95% prediction interval for the overall summary effect. Heterogeneity statistics (I^2 and *p*-value) are provided for each subgroup.

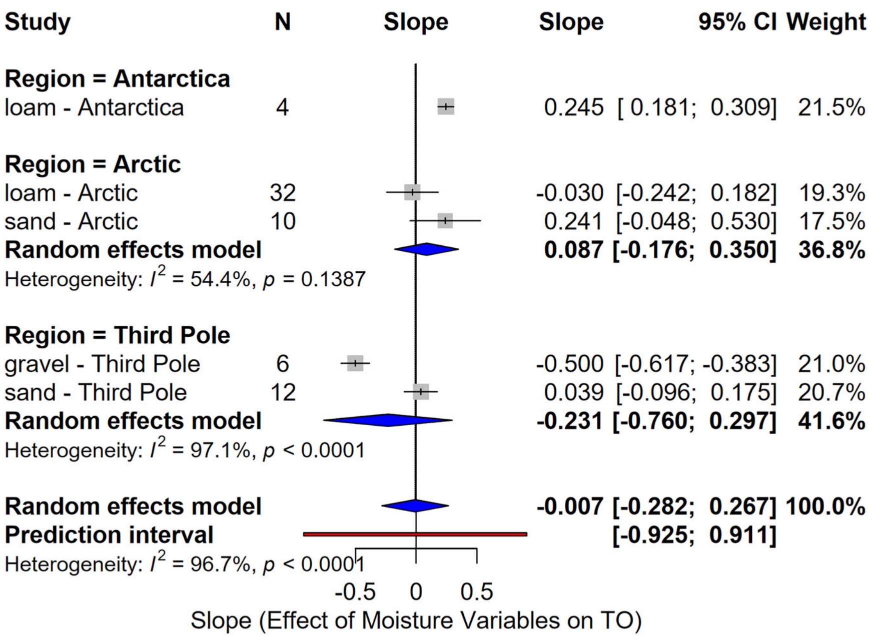

significantly positive, consistent with the 'balch effect' in coarse debris[65]. For example, the *TO* is 0.7 °C at the ELH site (coarse sand) but only 0.3 °C at the MDX3 site (fine-grained sand) (Fig. 4). In contrast, sites with clay soils exhibit a consistently negative *TO* (mean: −0.7 °C). The high water-retention capacity of clay leads to a significantly higher thermal conductivity when frozen than thawed, resulting in a large negative offset. Organic soils like peat introduce further complexity, where non-conductive processes such as subsurface water flow can counteract or even reverse the expected conductive offset. This is exemplified by the peat-covered CLP1 site, which has a positive *TO* of 0.4 °C (*MAGST* = − 2.3 °C, *TTOP* = − 1.9 °C), highlighting these complex interactions.

In the ultraxerous permafrost of Antarctica, local substrate properties exert a more pronounced control over the *TO*. Here, in hyper-arid environments where soils are predominantly coarse-grained mineral substrates, subtle variations in soil composition become a primary determinant of subsurface thermal dynamics. For example, minor differences in particle size distribution, such as the inclusion of fine sandy loam within a coarse gravelly matrix, can drive an order-of-magnitude difference in the observed *TO* (e.g., 1.4 °C versus 0.2–0.3 °C). Furthermore, the expected relationship between *TO* and *ALT* breaks down in this extreme environment. Although Antarctica has the lowest mean *ALT* (41.3 ± 5.5 cm), there is no consistent correlation with the *TO*. The Mt. Fleming site exemplifies this deviation: it exhibits one of the coldest thermal states globally (*TTOP*: −23.3 °C; *MAGST*: −23.5 °C) and the thinnest *ALT* (7.7 cm), yet its *TO* is slightly positive (0.2 °C). This pattern indicates that *ALT* alone is insufficient to explain *TO* variations here. Instead, Antarctic permafrost thermal dynamics appear to be governed more fundamentally by an interplay of substrate composition, the surface radiative balance, and non-conductive heat transfer within features like ice-rich debris or moraines.

While this conductive framework is well-established, its limitations in fully explaining the complexity of *TO* have been recognized[20,66]. Our data-driven analysis further confirms this, showing that its predictive power is highly context-dependent and often superseded by other processes. The meta-analysis reveals a weak, non-significant overall trend (slope = −0.007) that masks strong, opposing patterns when stratified by soil type (Fig. 7). The clearest alignment with conductive theory appears in the gravelly soils of the Third Pole, which exhibit a strong, significant negative slope (−0.50). This robustly confirms that higher moisture enhances winter heat loss as expected[30]. This contrasts sharply with the behavior of loamy soils, which, though theoretically prone to a negative *TO*, show a diametrically opposed response: a strong, significant positive slope in Antarctica (slope = 0.25) versus a weak negative trend in the Arctic. This reversal powerfully demonstrates that regional climatic regimes can override the expected thermal behavior of a given soil, likely due to the dominance of non-conductive heat transfer, such as the thermally-driven convection observed in coarse materials at Mt. Fleming site, Antarctica. Sandy soils further challenge a purely conductive view, with a consistently positive trend that suggests non-conductive processes like vapor diffusion may be a common, underappreciated mechanism in coarse-grained soils. Collectively, these findings demonstrate that the influence of moisture on *TO* is not monolithic. Instead, it is governed by an intricate interplay between substrate properties and the prevailing regional energy regime, which demands soil-specific parameterizations in permafrost models.

Taken together, our analysis demonstrates that the partitioning of energy fluxes within the active layer is governed by an intricate interplay between soil texture, dynamic moisture content, and the prevailing regional energy regime. While these mechanisms are often framed in terms of steady-state conductive balance, it is equally important to recognize that many observed *TO* values may reflect transient, non-equilibrium conditions. In such cases, permafrost temperatures can lag behind changes in surface conditions, resulting in the persistence of warmer permafrost than predicted by equilibrium models[46]. Such disequilibrium effects likely contribute to the regional and soil-type variations in *TO* identified here. This underscores the critical need to incorporate transient thermal dynamics and phase-change lag effects into next-generation permafrost modeling frameworks to improve projections of permafrost response to environmental change[67,68].

In conclusion, our cross-polar synthesis reveals that the permafrost thermal state is governed by a fundamental paradigm of scale-dependent decoupling of controls. We demonstrate that while the *SO* is controlled by large-scale climatic forcing like precipitation, the subsurface *TO* is fine-tuned by a context-dependent interplay of local substrate properties, where the influence of moisture can even reverse its thermal effect depending on the regional climate and soil texture. Failing to account for these substrate-specific, non-linear processes will lead to significant errors in projecting permafrost degradation, with major implications for global carbon cycling, hydrological connectivity, and infrastructure stability. Therefore, advancing predictive understanding of permafrost thermal dynamics requires a targeted, multi-pronged effort. This

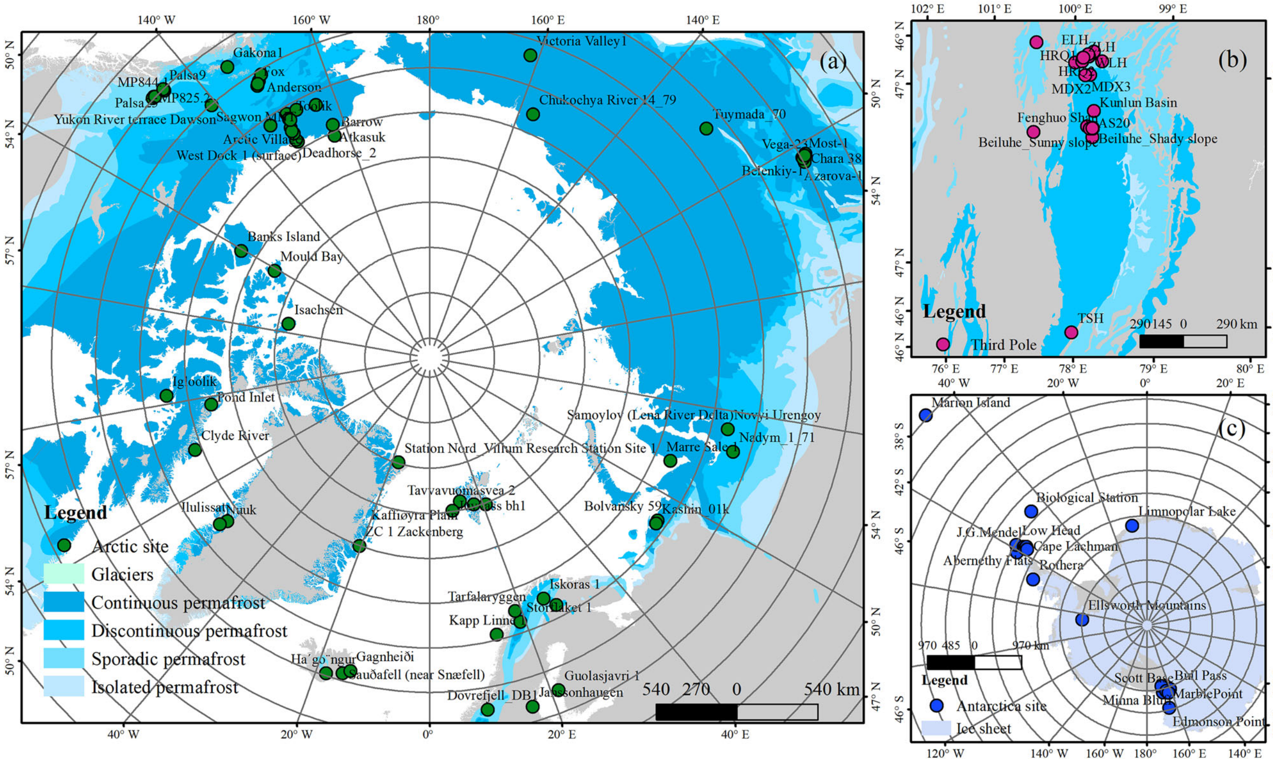

Fig. 8 | Overview of permafrost distribution and selected sites. This figure displays the global permafrost distribution (derived from the International Permafrost Association) and highlights selected study sites across the Arctic (**a**), Third Pole (**b**), and Antarctica (**c**). All maps are presented using polar projections, with geographic coordinates indicated by the grid lines.

includes: (1) expanding high-resolution monitoring networks, particularly in data-sparse regions, and crucially, maintaining long-term observations to quantify interannual variability; (2) improving the process-based representation of coupled snow-vegetation-soil thermal dynamics in numerical models, including transient responses to disturbances like wildfire in relevant biomes; and (3) integrating these models with remote sensing observations to upscale site-level understanding to regional and global scales. Ultimately, bridging the gap between large-scale climatic drivers and micro-scale substrate responses is not merely an academic challenge; it is critical for accurately forecasting the fate of permafrost in a warming world and its profound consequences for the global climate, ecosystems, and human societies.

Methods

Study sites and data compilation

This study synthesizes ground temperatures across 117 sites in the Arctic, Antarctica, and the Third Pole (Fig. 8). These sites represent diverse permafrost conditions categorized for regional comparison as cold-humid (Arctic), warm-dry (Third Pole), and cold-arid/ultraxerous (Antarctica). The Arctic dataset includes sites from the north slopes of the Alaska Range ($n = 18$), Canada ($n = 14$), Russia ($n = 15$), Nordic countries ($n = 11$), Svalbard ($n = 4$), and Greenland ($n = 4$) (Fig. 8a). The Third Pole representation comprises 32 sites that exhibit warm-dry permafrost characteristics (Fig. 8b). The Antarctic dataset includes 19 sites characterized by ultraxerous permafrost conditions (Fig. 8c). We compiled data for all sites of hourly *GST* (0–5 cm), hourly *Ta*, and *ALT*. Additionally, to represent the thermal conditions near the permafrost table, we also included hourly ground temperature from depths selected based on the site-specific *ALT*. These datasets were primarily compiled from documentations, the Global Terrestrial Network for Permafrost (GTN-P) dataset, and the Circumpolar Active Layer Monitoring (CALM) program archives (see Table 1 for a complete list of data sources).

Temperature offsets are defined by *MAGST*, *MAAT*, and *TTOP*. To investigate potential drivers of variability in temperature offsets, a comprehensive set of ancillary data was collected for each site. A total of sixteen variables were compiled as predictors for our machine learning models. Twelve of these predictors were derived from the ERA5-Land daily aggregated product, for which we calculated the long-term mean over a 10-year period (2014–2023). These variables represent key environmental processes, encompassing the cryosphere characteristics (e.g., snow depth, snow density, snow cover), hydrosphere components (e.g., 0–10, 10–40, 40–100, and 100–200 cm depth soil moisture, total precipitation, evaporation from vegetation transpiration), and the land-atmosphere interface (e.g., albedo, leaf area index, and 10 m wind components). The ERA5-Land dataset, which contains a total of 50 variables describing the global water and energy cycles over land hourly at a spatial resolution of 9 km[69], was accessed and processed using the Google Earth Engine (GEE) platform. Site-specific metadata provided the remaining quantitative predictors and the qualitative variables required for stratified analysis. The four quantitative predictors included the site's geographic coordinates (latitude and longitude), elevation, and the measured *ALT*.

Concurrently, qualitative information on vegetation type and soil texture was compiled specifically to facilitate the subsequent meta-analysis by serving as grouping variables. To ensure consistent analysis, original site descriptions were harmonized into standardized categories. For instance, sites described as polar desert, alpine desert, or barren land were grouped into a single "No vegetation" category. Similarly, detailed soil classifications were aggregated into five primary texture classes: loam (e.g., sandy loam, silt loam), sand (e.g., loamy sand, clay sand), gravel (e.g., sandy gravel, gneiss), peat, and clay (e.g., silty clay, sandy clay).

Temperature offsets

The thermal regime of permafrost is characterized by distinct temperature offsets between the atmosphere, the ground surface, and the top of the

Table 1 | Site information across the three poles

No.	Region	Sub-region	Site	MAGST	TTOP	ALT	MAAT	TO	SO	Note
1.	Arctic	Alaska	Anaktuvuk Pass	−4.7	−6.6	28.4	−6.67	−1.9	2.0	
2.	Arctic	Alaska	Anderson	0.2	1.7	98.0	−3.2	1.5	3.4	
3.	Arctic	Alaska	Arctic Village	−3.2	−3.4	103.0	−8.0	−0.2	4.8	
4.	Arctic	Alaska	Atkasuk	−3.9	−5.1	48.8	−8.4	−1.1	4.4	https://www.nrcs.usda.gov/
5.	Arctic	Alaska	Barrow	−6.5	−6.2	32.8	−11.1	0.2	4.6	
6.	Arctic	Alaska	Bonanza_Creek	0.5	−1.6	92.2	−3.1	−2.1	3.6	
7.	Arctic	Alaska	Chandalar_Shelf	−2.2	−3.4	37.4	−7.4	−1.2	5.2	
8.	Arctic	Alaska	Deadhorse_2	−3.2	−3.8	65.1	−11.1	−0.6	7.9	
9.	Arctic	Alaska	Fox	0.7	−0.5	84.7	−3.0	−1.3	3.8	
10.	Arctic	Alaska	Franklin_Bluffs	−3.9	−4.4	61.9	−10.6	−0.5	6.7	
11.	Arctic	Alaska	Gakona1	0.0	−1.0	62.0	−4.3	−1.1	4.4	
12.	Arctic	Alaska	Galbraith Lake*	−4.9	−4.7	49.8	−9.5	0.1	4.7	
13.	Arctic	Alaska	Happy Valley 1_b	−3.8	−4.5	39.9	−7.3	−0.7	3.5	
14.	Arctic	Alaska	Ivotuk_4	−2.6	−2.6	53.2	−10.1	−0.1	7.5	
15.	Arctic	Alaska	Sagwon MNT	−5.4	−5.3	55.1	−8.5	0.1	3.1	
16.	Arctic	Alaska	Smith Lake 3	2.9	0.1	76.8	−3.4	−2.8	6.3	
17.	Arctic	Alaska	Toolik	−5.3	−4.1	45.1	−8.0	1.2	2.7	https://www.nrcs.usda.gov/
18.	Arctic	Alaska	West Dock 1 (surface)	−4.5	−5.3	45.1	−9.2	−0.8	4.6	
19.	Arctic	Russia	Azarova−1	−8.8	−7.0	50.0	−9.3	1.8	0.5	
20.	Arctic	Russia	Belenkiy−1	−5.2	−6.6	53.9	−8.7	−1.4	3.5	
21.	Arctic	Russia	Bolvansky 59	−0.01	−0.4	112.9	−2.1	−0.4	2.0	
22.	Arctic	Russia	Chara 38	−3.9	−4.6	51.0	−5.7	−0.8	1.8	
23.	Arctic	Russia	Chukochya River 14_79	−15.0	−16.0	52.0 a	−15.0	−1.0	0.0	a:[74]
24.	Arctic	Russia	Kashin_01k	0.2	−0.4	73.6	−2.0	−0.5	2.1	
25.	Arctic	Russia	Marre Sale 1	1.4	−0.4	121.8	−7.0 a	−1.8	8.4	a:[75]
26.	Arctic	Russia	Most−1	−6.1	−7.1	48.8	−6.9	−0.9	0.7	
27.	Arctic	Russia	Nadym_1_71	3.2	−0.6	131.3	−2.6	−3.7	5.7	
28.	Arctic	Russia	Novyi Urengoy	−0.1	0.0	75.2	−7.5 a	0.1	7.4	a:[58]
29.	Arctic	Russia	Samoylov (Lena River Delta)	−9.1	−7.7	52.0	−12.5 a	1.4	3.4	a:[76]
30.	Arctic	Russia	Tuymada_70	−1.4	−1.4	200.8	−7.3 a	−0.1	6.0	a:[77]
31.	Arctic	Russia	Ushelistiy−1	−3.9	−5.0	51.4	−8.3	−1.2	4.5	
32.	Arctic	Russia	Vega−23	−5.0	−4.6	51.4	−6.5	0.5	1.6	
33.	Arctic	Russia	Zagryazkin−1	−3.6	−6.3	57.1	−5.0	−2.7	1.4	
34.	Arctic	Canada	Aggradational permafrost mound 1	−0.1 a	−0.8 a	177.0 a	−3.3 a	−0.7	3.2	a:[68]
35.	Arctic	Canada	Banks Island	−11.3	−11.4	60.0 a	−13.4	−0.1	2.1	a:[78]
36.	Arctic	Canada	Clyde River	−5.2	−5.3	100.0 a	−12.8	0.0	7.6	a:[79]
37.	Arctic	Canada	Fan (Coal Ridge logger site 2)	−0.4	−0.8	75.0	−3.6	−0.4	3.2	
38.	Arctic	Canada	Igloolik	−5.4	−6.0	120.0 a	−13.2	−0.7	7.9	a:[79]
39.	Arctic	Canada	Isachsen	−13.9	−13.2	54.2 a	−16.0	0.8	2.0	a:[80]
40.	Arctic	Canada	Mould Bay	−13.9	−13.8	52.8a	−14.9	0.1	1.0	a:[81]
41.	Arctic	Canada	MP825.2	1.7 a	0.0 a	100.0 a	−1.7 a	−1.7	3.4	a:[68]
42.	Arctic	Canada	MP844.1	1.1 a	0.0 a	100.0 a	−2.6 a	−1.1	3.7	a:[68]
43.	Arctic	Canada	Mt McIntyre	−0.8 a	−1.2 a	700.0 a	−2.5 a	−0.4	1.7	a:[68]
44.	Arctic	Canada	Palsa25	0.8 a	−0.5 a	100.0 a	−3.3 a	−1.3	4.1	a:[68]
45.	Arctic	Canada	Palsa9	1.3 a	−0.7 a	70.0 a	−2.1 a	−2.0	3.4	a:[68]
46.	Arctic	Canada	Pond Inlet	−6.0	−6.5	190.0 a	−7.6	−0.6	1.6	a:[79]
47.	Arctic	Canada	Yukon River terrace Dawson	−0.7 a	−2.9 a	75.0 a	−4.1 a	−2.2	3.4	a:[68]
48.	Arctic	Greenland	Ilulissat	−4.4 a	−3.0 a	80.0 a	−3.9 a	1.4	−0.5	a:[82]
49.	Arctic	Greenland	Nuuk	0.9 a	−1.0 a	90.0 a	−1.9 a	−1.9	2.8	a:[82]
50.	Arctic	Greenland	Station Nord_Villum Research Station Site 1	−8.7 a	−6.2 a	88.7a	−13.7 a	2.4	5.3	a:[83]
51.	Arctic	Greenland	ZC 1 Zackenberg	−5.5 a	−7.3 a	79.4 a	−9.5 a	−1.8	4.0	a:[84]

Table 1 (continued) | Site information across the three poles

No.	Region	Sub-region	Site	MAGST	TTOP	ALT	MAAT	TO	SO	Note
52.	Arctic	Nordic	Dovrefjell_DB1	−1.1 a	−0.2 a	8.5 a	−1.6 a	0.9	0.5	a:[85]
53.	Arctic	Nordic	Gagnheiði	−0.7 a	−0.5 a	450.0 a	−1.4 a	0.2	0.7	a:[82]
54.	Arctic	Nordic	Guolasjavri 1	−0.7 a	0.0 a	1000.0a	−2.1 a	0.7	1.4	a:[82]
^{5}5.	Arctic	Nordic	Ha´go¨ngur	0.2 a	0.0 a	1000.0a	0.4 a	−0.2	−0.2	a:[82]
^{5}6.	Arctic	Nordic	Iskoras 1	−0.5 a	0.0 a	700.0 a	−0.5 a	0.5	0.0	a:[82]
57.	Arctic	Nordic	Juvvass bh1	−2.4 a	−2.2 a	150.0 a	−3.3 a	0.2	0.9	a:[82]
58.	Arctic	Nordic	Kevo(Valsjeaggl 1)	−0.6 a	−2.0 a	60.0 a	−1.0 a	−1.4	0.4	a:[82]
59.	Arctic	Nordic	Sauðafell (near Snæfell)	−0.6 a	−1.0 a	200.0 a	−1.3 a	−0.4	0.7	a:[82]
60.	Arctic	Nordic	Storflaket 1	−0.4 a	−0.4 a	80.9 a	−1.7 a	0.0	1.3	a:[86]
61.	Arctic	Nordic	Tarfalaryggen	−3.4 a	−3.0 a	160.0 a	−4.6 a	0.4	1.2	a:[82]
62.	Arctic	Nordic	Tavvavuoma	0.2 a	−1.0 a	50.0 a	−1.7 a	−1.2	1.9	a:[82]
63.	Arctic	Svalbard	Janssonhaugen	−5.6 a	−5.5 a	170.0 a	−6.0 a	0.1	0.4	a:[82]
64.	Arctic	Svalbard	Kaffiøyra Plain	6 a	1.85 a	134.75a	4.63 a	−4.15	1.38	a:[86]
65.	Arctic	Svalbard	Kapp Linne 1	−3.2 a	−3.8 a	250.0 a	−3.4 a	−0.6	0.2	a:[82]
66.	Arctic	Svalbard	svea 2	−4.3 a	−3.5 a	200.0 a	−5.0 a	0.8	0.7	a:[82]
67.	Third Pole	Tibetan Plateau	AS20	−0.6 a	−1.3 a		−3.6 a	−0.7	3.3	a:[87]
68.	Third Pole	Tibetan Plateau	Beiluhe_Alpine desert	0.7 a	−0.1 a		−2.8 a	−0.7	3.5	a:[88]
69.	Third Pole	Tibetan Plateau	Beiluhe_Alpine grassland	0.6 a	−0.1 a		−3.0 a	−0.8	3.6	a:[88]
70.	Third Pole	Tibetan Plateau	Beiluhe_Alpine meadow	0.3 a	−0.4 a		−2.8 a	−0.7	3.2	a:[88]
71.	Third Pole	Tibetan Plateau	Beiluhe_Shady slope	−0.5 a	−1.2 a		−2.7 a	−0.7	2.2	a:[88]
72.	Third Pole	Tibetan Plateau	Beiluhe_Sparse grassland	0.4 a	−0.1 a		−3.0 a	−0.5	3.4	a:[88]
73.	Third Pole	Tibetan Plateau	Beiluhe_Sunny slope	0.8 a	0.3 a		−2.8 a	−0.6	3.6	a:[88]
74.	Third Pole	Tibetan Plateau	Beiluhe_Swamp meadow	0.7 a	−0.2 a		−3.2 a	−0.9	3.9	a:[88]
75.	Third Pole	Tibetan Plateau	Beiluhe_Transitional area	0.5 a	0.5 a		−2.9 a	−0.1	3.4	a:[88]
76.	Third Pole	Tibetan Plateau	CLP1	−2.3 a	−1.9 a		−4.5 a	0.4	2.2	a:[25]
77.	Third Pole	Tibetan Plateau	CLP2	−2.2 a	−2.0 a		−4.4 a	0.2	2.2	a:[25]
78.	Third Pole	Tibetan Plateau	CLP3	−3.0 a	−2.3 a		−4.2 a	0.6	1.3	a:[25]
79.	Third Pole	Tibetan Plateau	ELH	0.4 a	1.2 a		−2.7 a	0.7	3.1	a:[25]
80.	Third Pole	Tibetan Plateau	Fenghuo Shan	0.0 a	−0.3 a	143.0 b	−6.1 a	−0.3	6.1	a:[89]; b:[90]
81.	Third Pole	Tibetan Plateau	Heihe River Basin_AL7	0.3 a	0.4 a	39.0 a	−4.1 a	0.1	4.4	a:[91]
82.	Third Pole	Tibetan Plateau	Heihe River Basin_EB	0.3 a	−1.2 a	80.0 a	−2.4 a	−1.5	2.7	a:[91]
83.	Third Pole	Tibetan Plateau	HRQ1	0.0 a	−0.5 a		−3.3 a	−0.5	3.3	a:[25]
84.	Third Pole	Tibetan Plateau	HRQ2	−0.7 a	−0.9 a		−3.2 a	−0.2	2.5	a:[25]
85.	Third Pole	Tibetan Plateau	Kunlun Basin	0.0 a	−0.4 a	136.0 b	−5.8 a	−0.4	5.8	a:[89]; b:[90]
86.	Third Pole	Tibetan Plateau	MDX1	−0.8 a	−0.3 a		−3.6 a	0.6	2.7	a:[25]
87.	Third Pole	Tibetan Plateau	MDX2	0.2 a	−0.3 a		−3.6 a	−0.5	3.8	a:[25]
88.	Third Pole	Tibetan Plateau	MDX3	−0.5 a	−0.2 a		−2.8 a	0.3	2.3	a:[25]
89.	Third Pole	Tibetan Plateau	QSH1	−1.1 a	0.9 a		−3.2 a	2.0	2.2	a:[25]
90.	Third Pole	Tibetan Plateau	TCM1	−0.4 a	−0.9 a		−2.7 a	−0.5	2.4	a:[25]
91.	Third Pole	Tibetan Plateau	TCM2	0.0 a	−0.4 a		−2.8 a	−0.4	2.8	a:[25]
92.	Third Pole	Tibetan Plateau	TSH	−3.2 a	−2.2 a		−7.6 a	1.00	4.4	a:[25]
93.	Third Pole	Tibetan Plateau	WLH	−0.8 a	−1.4 a		−3.7 a	−0.6	2.9	a:[25]
94.	Third Pole	Tibetan Plateau	Wudaoliang Basin _Meadow	−0.9 a	−1.3 a	212.5 a	−4.0 a	−0.4	3.1	a:[102]
95.	Third Pole	Tibetan Plateau	Wudaoliang Basin _Rock grid	−1.0 a	−1.8 a	164.5 a	−4.0 a	−0.8	3.0	a:[102]
96.	Third Pole	Tibetan Plateau	Wudaoliang Basin _Sprasely vegetated area	−0.5 a	−0.5 a	250.5 a	−4.0 a	0.0	3.5	a:[102]
97.	Third Pole	Tibetan Plateau	Wudaoliang Basin _Transition	−0.6 a	−1.3 a	221.5 a	−4.0 a	−0.7	3.4	a:[102]
98.	Third Pole	Tibetan Plateau	ZLH	−0.6 a	−0.9 a		−1.9 a	−0.3	1.2	a:[25]
99.	Antarctica	Antarctica	Abernethy Flats	−6.1 a	−6.2 a		−7.3 a	−0.1	1.2	a:[92]
100.	Antarctica	Antarctica	Berry Hill slopes	−6.4 a	−6.4 a		−7.1 a	−0.1	0.8	a:[93]
101.	Antarctica	Antarctica	Biological Station	−2.4 a	−2.6 a		−3.8 a	−0.2	1.4	a:[44]
102.	Antarctica	Antarctica	Bull Pass	−17.4	−17.7	49.8	−18.0	−0.2	0.5	https://www.nrcs.usda.gov/
103.	Antarctica	Antarctica	Cape Lachman	−4.5 a	−4.7 a		−5.8 a	−0.2	1.3	a:[94]

Table 1 (continued) | Site information across the three poles

No.	Region	Sub-region	Site	MAGST	TTOP	ALT	MAAT	TO	SO	Note
104.	Antarctica	Antarctica	Deception Island	−2.2 a	−2.0 a	54.1	−3.0 a	0.1	0.8	a:[95]
105.	Antarctica	Antarctica	Edmonson Point	−14.7 a	−14.3 a		−16.4 a	0.4	1.8	a:[96]
106.	Antarctica	Antarctica	Ellsworth Mountains	−18.3 a	−18.3 a		−19.8 a	0.0	1.5	a:[97]
107.	Antarctica	Antarctica	Granite Harbour	−14.8	−14.3	85.1	−16.4	0.5	1.5	https://www.nrcs.usda.gov/
108.	Antarctica	Antarctica	J.G.Mendel	−5.6 a	−5.7 a		−6.7 a	−0.1	1.1	a:[98]
109.	Antarctica	Antarctica	Limnopolar Lake	−0.9 a	−0.9 a		−2.5 a	0.0	1.6	a:[99]
110.	Antarctica	Antarctica	Low Head	−1.5 a	−1.6 a		−3.1 a	−0.1	1.6	a:[100]
111.	Antarctica	Antarctica	MarblePoint	−17.9	−18.1	50.0	−17.7	−0.2	−0.2	https://www.nrcs.usda.gov/
112.	Antarctica	Antarctica	Marion Island	2.6 a	0.6 a		3.0 a	−2.0	−0.40	a:[101]
113.	Antarctica	Antarctica	Minna Bluff	−16.9	−16.9	26.9	−18.4	0.0	1.5	https://www.nrcs.usda.gov/
114.	Antarctica	Antarctica	Mt. Fleming	−23.5	−23.3	7.7	−24.0	0.2	0.5	https://www.nrcs.usda.gov/
115.	Antarctica	Antarctica	Rothera	−3.7 a	−3.0 a		−3.0 a	0.6	−0.7	a:[53]
116.	Antarctica	Antarctica	Scott Base	−17.2	−17.2	34.3	−18.6	0.0	1.4	https://www.nrcs.usda.gov/
117.	Antarctica	Antarctica	Victoria Valley1	−23.0	−22.7	22.2	−23.3	0.3	0.3	https://www.nrcs.usda.gov/

Columns are defined as: *MAGST* (mean annual ground surface temperature, °C); *TTOP* (temperature at the top of permafrost, °C); *ALT* (active layer thickness, cm); *MAAT* (mean annual air temperature, °C); *TO* (thermal offset, °C); *SO* (surface offset, °C); and Note (additional information or source). For the *MAGST*, *MAAT*, *TTOP*, and *ALT* columns, data are primarily sourced from the Global Terrestrial Network for Permafrost (GTN-P) and the Circumpolar Active Layer Monitoring (CALM) program, except where a specific source is provided in the "Note" column.

permafrost. *SO* is defined as the difference between *MAGST* and *MAAT*:

$$SO = MAGST - MAAT \tag{1}$$

SO reflects the net thermal influence of the ground surface energy balance components, primarily modulated by surface characteristics[20]. In winter, insulating layers like snow cover and organic soil horizons decouple the ground surface from cold air temperatures, typically leading to $MAGST > MAAT$. The thickness, density, and duration of snow cover are major controls on ground surface thermal regimes. In summer, factors like vegetation cover (shading, altered albedo, evapotranspiration) and the thermal properties of the surface organic layer influence energy absorption and partitioning, further contributing to the offset.

TO refers to the difference between *MAGST* and *TTOP*:

$$TO = TTOP - MAGST \tag{2}$$

The temporal coverage of the data used to calculate *TO* and *SO* varied among sites and regions (Supplementary Figs. 1–6). *TO* is primarily influenced by variations in thermal conductivity between the thawed (humid) and frozen (ice-rich or dry) states of the active layer soils[70]. Typically, thermal conductivity is higher in the frozen state (K_f) than in the thawed state (K_t), especially in unsaturated soils. This asymmetry ($K_f > K_t$) leads to more efficient heat loss from soils during winter compared to heat gain during summer, resulting in a colder *TTOP* than *MAGST*. Latent heat effects associated with the phase change of water within the active layer also contribute significantly to this offset, damping temperature fluctuations near 0 °C.

Descriptive analysis of temperature offsets

To characterize the spatial distribution and variability of temperature offsets across different permafrost regions and spatial scales, several descriptive analyses and visualizations were conducted. To synthesize the thermal characteristics and their variability across different permafrost regions, descriptive statistics (mean ± standard error) were calculated for *MAAT, MAGST, TTOP, TO*, and *SO*, for sites grouped into defined sub-regions (e.g., Alaska, Russia, Greenland, Svalbard, Tibetan Plateau, Antarctica, Nordic, Canada) within the three major permafrost regions. These regional summaries were visualized using forest plots generated with the *ggforestplot* package (v0.1.0) to allow inter-regional comparison of mean offset magnitudes and associated temperatures. The spatial distribution of mean site-specific *TO* and *SO* values (mean across all available years per site) was illustrated on global maps, with marker size representing the absolute magnitude of the offset ($|TO|$ or $|SO|$) and marker color indicating the signed value (positive or negative offset).

Furthermore, representative mean annual temperature-depth profiles from select sites within the Arctic, Antarctic, and the Third Pole were presented to visualize the vertical thermal regime and illustrate the differences in key thermal parameters (*MAAT, MAGST, TTOP, ALT, SO*, and *TO*) across the three poles. To quantify the relative variability of *TO* and *SO* within each of the three major permafrost regions, the coefficient of variation (*CV*) was calculated. The *CV*, defined as the ratio of the standard deviation (σ) to the mean (μ), quantifies relative variability and is expressed as a percentage[71]:

$$CV = \frac{\sigma}{\mu} \times 100\% \tag{3}$$

XGBoost and SHAP analysis of multivariate drivers

To quantify the influence of multiple environmental factors on *TO* and *SO*, we employed the XGBoost algorithm[72] coupled with Shapley additive explanations (SHAP)[73] for model interpretation. The cleaned and preprocessed dataset was randomly split into training (75%) and testing (25%) subsets to facilitate model development and evaluation. The training data were used to develop the models, while the testing set served as a holdout for monitoring performance and preventing overfitting via early stopping. Separate XGBoost regression models were developed to predict *TO* and *SO* using the 16 predictive variables detailed in the preceding section as input features. Models were trained using the "reg: squarederror" objective and "rmse" evaluation metric, with hyperparameters (e.g., eta = 0.1, max_depth = 6) tuned to optimize performance. Early stopping (patience = 10) was employed over up to 100 boosting rounds to prevent overfitting. An XGBoost model, as an ensemble of K decision trees (f_k), maps feature x to a prediction $\hat{y}$:

$$\hat{y} = f(x) = \sum_{k=1}^{K} f_k(x) \tag{4}$$

To interpret the model predictions, SHAP values were calculated for all training samples in the training set using the *predict ()* function with the *predcontrib = TRUE* argument, which implements the TreeSHAP algorithm. These values attribute the difference between a prediction $f(x)$ and the expected output $E\left[f(X)\right]$ to each feature i, satisfying the additivity property:

$$f(x) = E\left[f(X)\right] + \sum_{i=1}^{M} \varphi_i(x) \tag{5}$$

where M is the number of features and $\varphi_i(x)$ is the SHAP value for feature i and input x. $\varphi_i(x)$ represents the contribution of feature i to the prediction for instance x relative to the mean prediction. SHAP values were computed using the TreeSHAP algorithm in the *xgboost* package.

To assess feature importance and typical influence direction, SHAP values were summarized across training samples. Global importance of feature i was quantified by the mean absolute SHAP value:

$$Importance_i = \frac{1}{N}\sum_{j=1}^{N} |\varphi_i\left(x_j\right)| \tag{6}$$

The typical directional influence was assessed by the mean signed SHAP value:

$$Directional\ Influence_i = \frac{1}{N}\sum_{j=1}^{N} \varphi_i\left(x_j\right) \tag{7}$$

where N is the number of training samples. These importance scores, along with mean feature values and mean signed SHAP values, were compiled to evaluate the contribution of each predictor to both the *TO* and *SO* models.

All modeling and SHAP analyses were conducted in R (v4.3.2) using the *xgboost*, *dplyr*, *ggplot2*, and *patchwork* packages.

Meta-analysis

We employed a meta-analysis approach to examine the influence of key environmental drivers on the changing magnitudes of *TO* and *SO* across different permafrost sites. Two separate analyses were conducted: one for the effect of snow-related variables (snow depth, density, and cover) on *SO*, and another for the effect of moisture-related variables (total precipitation and volumetric soil water at four depths) on *TO*. Each unique combination of site characteristics (vegetation type for the snow analysis; soil texture for the moisture analysis) within a specific geographic region was treated as an individual study in the meta-analysis. For each study, we first quantified the local driver-response relationship. Recognizing that these related predictors are often collinear, we used a principal component analysis (PCA) to derive a single composite predictor representing their dominant mode of variation. The relationship was then quantified by fitting a simple linear regression model:

$$Off\ set_j = \alpha_j + \beta_j Predict_j + \varepsilon_j \tag{8}$$

where $Predict_j$ is either the first principal component (PC1) score or the single varying driver for study j. In all cases, the estimated regression slope ($\hat{\beta}_j$) and its standard error ($\mathrm{se}(\hat{\beta}_j)$) were extracted to serve as the effect size and its variance estimate, respectively. Groups with insufficient data points for a stable regression were excluded from the meta-analysis.

Given the expected considerable spatial heterogeneity in permafrost thermal regimes and environmental controls across diverse regions and surface characteristics, a random-effects model was chosen for the meta-analysis. This model assumes that the true effect size (slope, β_j) for each group j is not identical but varies around an overall mean effect (μ) with a between-group variance (τ^2), reflecting true heterogeneity beyond sampling error. The observed effect size ($\hat{\beta}_j$) for group j is therefore modeled as:

$$\hat{\beta}_j = \beta_j + \varepsilon_j \tag{9}$$

where $\beta_j \sim N(\mu, \tau^2)$ represents the distribution of true effects, and $\varepsilon_j \sim N(0, \mathrm{se}(\hat{\beta})^2)$ represents the sampling error from the local regression. The random-effects model provides a pooled estimate ($\hat{\mu}$) that is a weighted mean of the true effects, accounting for both within-study sampling variability and between-group heterogeneity.

Heterogeneity among the true effects (β_j) was assessed using Cochran's Q statistic and formally quantified by the I^2 statistic, which estimates the percentage of total variation across groups attributable to true heterogeneity rather than sampling error. The formula for I^2 is:

$$I^2 = \frac{Q - (k - 1)}{Q} \times 100\% \tag{10}$$

where Q is the Q-statistic and k is the number of groups included in the analysis.

Subgroup analysis was performed by geographic region to explore regional differences in the pooled effects for both models. All meta-analyses were conducted using the *metagen* function from the *meta* package in R (v4.3.2). Forest plots were generated to visualize the estimated effect size and confidence interval for each group, along with the pooled estimates for each regional subgroup and the overall random-effects pooled estimate and its prediction interval.

Data availability

This study is a synthesis based on existing, publicly available data. All data required to reproduce the findings are available from the sources described below. The original observational data underpinning this synthesis were compiled from the following publicly available archives and publications: (1) The Global Terrestrial Network for Permafrost (GTN-P) database, available at https://gtnp.arcticportal.org/. (2) The Circumpolar Active Layer Monitoring (CALM) program archives, available at https://www2.gwu.edu/~calm/. (3) The Antarctic Meteorological Research and Data Center (AMRDC), available at https://amrdcdata.ssec.wisc.edu/. (4) The USDA Natural Resources Conservation Service (NRCS), available at https://www.nrcs.usda.gov/, as referenced in Table 1. (5) Data from other specific sites are available through the original publications as cited in the "Note" column of Table 1. And the ancillary environmental data used for the machine learning models were derived from the ERA5-Land dataset, which is publicly available from the Copernicus Climate Change Service (C3S) Climate Data Store at https://cds.climate.copernicus.eu/.

Received: 3 July 2025; Accepted: 13 September 2025;
Published online: 05 November 2025

References

1. Muller, S. W. Permafrost or permanently frozen ground and related engineering problems. Army Map Service, US Army (1945).
2. Dobinski, W. Permafrost. *Earth Sci. Rev.* **108**, 158–169 (2011).
3. Gruber, S. Derivation and analysis of a high-resolution estimate of global permafrost zonation. *Cryosphere* **6**, 221–233 (2012).
4. Noetzli, J. et al. Enhanced warming of European mountain permafrost in the early 21st century. *Nat. Commun.* **15**, 10508 (2024).

5. Miner, K. R. et al. Permafrost carbon emissions in a changing Arctic. *Nat. Rev. Earth Environ.* **3**, 55–67 (2022).
6. Smith, S. L., O'Neill, H. B., Isaksen, K., Noetzli, J. & Romanovsky, V. E. The changing thermal state of permafrost. *Nat. Rev. Earth Environ.* **3**, 10–23 (2022).
7. Zhao, L. et al. Investigation, monitoring, and simulation of permafrost on the Qinghai-Tibet Plateau: a review. *Permafr. Periglac. Process.* **35**, 412–422 (2024).
8. Luo, D. et al. Revised understanding of permafrost shape: inclusion of the transition zone and its climatic and environmental significances. *J. Earth Sci.* **36**, 339–346 (2025).
9. Luo, D., Liu, J., Chen, F. & Li, S. Observed talik development triggers a tipping point in marginal permafrost of the Qinghai-Xizang Plateau. *Geosci. Front.* **16**, 102122 (2025).
10. Wisser, D., Marchenko, S., Talbot, J., Treat, C. & Frolking, S. Soil temperature response to 21st century global warming: The role of and some implications for peat carbon in thawing permafrost soils in North America. *Earth Syst. Dyn.* **2**, 121–138 (2011).
11. Mu, C. et al. High carbon emissions from thermokarst lakes and their determinants in the Tibet Plateau. *Glob. Chang Biol.* **29**, 2732–2745 (2023).
12. Chi, H. et al. Influence of interspecies interactions on bacterial community assembly in the active and permafrost layers on the Qinghai-Tibet Plateau. *J. Earth Sci.* **36**, 395–407 (2025).
13. Jorgenson, M. et al. Resilience and vulnerability of permafrost to climate change. *Can. J. For. Res.* **40**, 1219–1236 (2010).
14. Painter, S. L., Coon, E. T., Khattak, A. J. & Jastrow, J. D. Drying of tundra landscapes will limit subsidence-induced acceleration of permafrost thaw. *Proc. Natl Acad. Sci. USA* **120**, e2212171120 (2023).
15. Kokelj, S. V. et al. The Northwest Territories Thermokarst Mapping Collective: a northern-driven mapping collaborative toward understanding the effects of permafrost thaw. *Arctic Sci.* **9**, 886–918 (2023).
16. Jin, X.-Y. et al. Impacts of climate-induced permafrost degradation on vegetation: a review. *Adv. Clim. Change Res.* **12**, 29–47 (2021).
17. Heijmans, M. M. P. D. et al. Tundra vegetation change and impacts on permafrost. *Nat. Rev. Earth Environ.* **3**, 68–84 (2022).
18. Hjort, J. et al. Impacts of permafrost degradation on infrastructure. *Nat. Rev. Earth Environ.* **3**, 24–38 (2022).
19. Ran, Y. et al. Permafrost degradation increases risk and large future costs of infrastructure on the Third Pole. *Commun. Earth Environ.* **3**, 238 (2022).
20. Smith, M. W. & Riseborough, D. W. Climate and the limits of permafrost: a zonal analysis. *Permafr. Periglac. Process.* **13**, 1–15 (2002).
21. Luo, D., Jin, H., Marchenko, S. S. & Romanovsky, V. E. Difference between near-surface air, land surface and ground surface temperatures and their influences on the frozen ground on the Qinghai-Tibet Plateau. *Geoderma* **312**, 74–85 (2018).
22. Brown, R. J. E. The distribution of permafrost and its relation to air temperature in Canada and the U.S.S.R. *Arctic* **13**, 163–177 (1960).
23. Hu, G. et al. Evaluation of reanalysis air temperature products in permafrost regions on the Qinghai-Tibetan Plateau. *Theor. Appl. Climatol.* **138**, 1457–1470 (2019).
24. Victor, S. Detection of increase in air temperature in Barrow, AK, USA, through the use of extreme value indices and its impact on the permafrost active layer thickness. *Theor. Appl. Climatol.* **148**, 79–89 (2022).
25. Luo, D. et al. Thermal regime of warm-dry permafrost in relation to ground surface temperature in the Source Areas of the Yangtze and Yellow rivers on the Qinghai-Tibet Plateau, SW China. *Sci. Total Environ.* **618**, 1033–1045 (2018).
26. Luo, D., Liu, L., Jin, H., Wang, X. & Chen, F. Characteristics of ground surface temperature at Chalaping in the Source Area of the Yellow River, northeastern Tibetan Plateau. *Agric. Forest Meteorol.* **281**, 107819 (2020).
27. Luo, D. L. et al. Characteristics of water-heat exchanges and inconsistent surface temperature changes at an elevational permafrost site on the Qinghai-Tibet Plateau. *J. Geophys. Res. Atmos.* **123**, 10057–10075 (2018).
28. Hoelzle, M. & Gruber, S. Borehole and ground surface temperatures and their relationship to meteorological conditions in the Swiss Alps. (2008).
29. Jorgenson, M. T., Douglas, T. A., Shur, Y. L. & Kanevskiy, M. Z. Mapping the vulnerability of boreal permafrost in central Alaska in relation to thaw rate, ground ice, and thermokarst development. *J. Geophys. Res. Earth Surf.* **130**, e2024JF008030 (2025).
30. Burn, C. & Smith, C. Observations of the "Thermal Offset" in near-surface mean annual ground temperatures at several sites near Mayo, Yukon Territory, Canada. *ARCTIC* **41**, 99–104 (1988).
31. Romanovsky, V. E. & Osterkamp, T. E. Interannual variations of the thermal regime of the active layer and near-surface permafrost in northern Alaska. *Permafr. Periglac. Process.* **6**, 313–335 (1995).
32. Riseborough, D. W. The mean annual temperature at the top of permafrost, the TTOP model, and the effect of unfrozen water. *Permafr. Periglac. Process.* **13**, 137–143 (2002).
33. French, H. & Shur, Y. The principles of cryostratigraphy. *Earth Sci. Rev.* **101**, 190–206 (2010).
34. Goodrich, L. E. Some results of a numerical study of ground thermal regimes. *Int. Conf. Permafr.* **1**, 29–34 (1978).
35. Murton, J. B. *Treatise on Geomorphology* 4 (ed J. Shroder, Haritashya) 428–457 (Academic Press, 2022).
36. Lacelle, D. et al. Permafrost and ground-ice conditions in the Untersee Oasis, Queen Maud Land, East Antarctica. *Antarct. Sci.* **36**, 361–378 (2024).
37. Lin, Z. et al. The thermal regime, including a reversed thermal offset, of arid permafrost sites with variations in vegetation cover density, Wudaoliang Basin, Qinghai-Tibet Plateau. *Permafr. Periglac. Process.* **26**, 142–159 (2015).
38. Pan, X. et al. Effects of stratified active layers on high-altitude permafrost warming: a case study on the Qinghai–Tibet Plateau. *Cryosphere* **10**, 1591–1603 (2016).
39. Guglielmin, M., Ellis Evans, C. J. & Cannone, N. Active layer thermal regime under different vegetation conditions in permafrost areas. A case study at Signy Island (Maritime Antarctica). *Geoderma* **144**, 73–85 (2008).
40. Romanovsky, V. E. & Osterkamp, T. E. Thawing of the active layer on the coastal plain of the Alaskan Arctic. *Permafr. Periglac. Process.* **8**, 1–22 (1997).
41. Kristensen, L. & Christiansen, H. Temperatures in coastal permafrost in the Svea Area, Svalbard. In *Proc. Ninth International Conference on Permafrost, Institute of Northern Engineering*, *University of Alaska Fairbanks* Vol. 1, 1005–1010 (2008).
42. Kotze, C. & Meiklejohn, I. Temporal variability of ground thermal regimes on the northern buttress of the Vesleskarvet nunatak, western Dronning Maud Land, Antarctica. *Antarct. Sci.* **29**, 1–9 (2016).
43. Hu, G. et al. Thermal properties of active layer in permafrost regions with different vegetation types on the Qinghai-Tibetan Plateau. *Theor. Appl. Climatol.* **139**, 983–993 (2020).
44. Guglielmin, M. & Cannone, N. A permafrost warming in a cooling Antarctica?. *Clim. Change* **111**, 177–195 (2012).
45. Smith, S. L. et al. Thermal state of permafrost in North America: a contribution to the International Polar Year. *Permafr. Periglac. Process.* **21**, 117–135 (2010).
46. James, M., Lewkowicz, A. G., Smith, S. L. & Miceli, C. M. Multi-decadal degradation and persistence of permafrost in the Alaska Highway corridor, northwest Canada. *Environ. Res. Lett.* **8**, 045013 (2013).

47. Palmer, M. J., Burn, C. R. & Kokelj, S. V. Factors influencing permafrost temperatures across tree line in the uplands east of the Mackenzie Delta, 2004–20101This article is one of a series of papers published in this CJES Special Issue on the theme of Fundamental and applied research on permafrost in Canada. 2Polar Continental Shelf Contribution 03611. *Can. J. Earth Sci.* **49**, 877–894 (2012).
48. Smith, S. L., Burgess, M. M., Riseborough, D. & Mark Nixon, F. Recent trends from Canadian permafrost thermal monitoring network sites. *Permafr. Periglac. Process.* **16**, 19–30 (2005).
49. Cheng, J.-j & Xue, C.-x. The sand-damage–prevention engineering system for the railway in the desert region of the Qinghai-Tibet plateau. *J. Wind Eng. Ind. Aerodyn.* **125**, 30–37 (2014).
50. Riseborough, D. W. & Smith, M. W. Exploring the limits of permafrost. In *Proc. 7th International Conference on Permafrost, Yellowknife Nordicana*, *Collection Nordicana No 55*, 935–942 (1998).
51. Throop, J., Lewkowicz, A. G. & Smith, S. Climate and ground temperature relations at sites across the continuous and discontinuous permafrost zones, northern Canada. *Can. J. Earth Sci.* **49**, 865–876 (2012).
52. Smith, R. I. L. Vegetation of the soviet polar deserts. *Trends Ecol. Evol.* **4**, 151 (1989).
53. Hrbáček, F. et al. Active layer and permafrost thermal regimes in the ice-free areas of Antarctica. *Earth Sci. Rev.* **242**, 104458 (2023).
54. Goodrich, L. E. The influence of snow cover on the ground thermal regime. *Can. Geotech. J.* **19**, 421–432 (1982).
55. Grünberg, I., Wilcox, E. J., Zwieback, S., Marsh, P. & Boike, J. Linking tundra vegetation, snow, soil temperature, and permafrost. *Biogeosciences* **17**, 4261–4279 (2020).
56. Loranty, M. et al. Reviews and syntheses: changing ecosystem influences on soil thermal regimes in northern high-latitude permafrost regions. *Biogeosci. Discuss.* **15**, 1–56 (2018).
57. Yoshikawa, K. et al. Ground thermal regimes and implications for permafrost distribution on Kilimanjaro, Tanzania. *Arct. Antarct. Alp. Res.* **53**, 127–145 (2021).
58. Romanovsky, V. et al. Thermal State of Permafrost in Russia. *Permafr. Periglac. Process.* **21**, 136–155 (2010).
59. Su, H., Zhong, X., Cao, B., Hu, Y., Zheng, L. & Zhang, T. Comparison of bulk snow density measurements using different methods. *Adv. Clim. Change Res* **15**, 658–668 (2023).
60. Christiansen, H. & Humlum, O. Interannual variations in active layer thickness in Svalbard. In *Proc. Ninth International Conference on Permafrost*, *Institute of Northern Engineering, University of Alaska Fairbanks* Vol. 1, 257–262 (2008).
61. Burn, C. R. & Please provide the complete information in ref, C. A. C. Observations of the “thermal offset” in near-surface mean annual ground temperatures at several sites near Mayo, Yukon Territory. *Can. Arct.* **41**, 99–104 (1988).
62. Cheng, G. Influences of local factors on permafrost occurrence and their implications for Qinghai-Xizang Railway design. *Sci. China Ser. D. Earth Sci.* **47**, 704–709 (2004).
63. Way, R. G., Lewkowicz, A. G. & Zhang, Y. Characteristics and fate of isolated permafrost patches in coastal Labrador, Canada. *Cryosphere* **12**, 2667–2688 (2018).
64. Du, R. et al. Response of peat-rich permafrost to a warming climate on the northeast Tibetan Plateau. *Agric. Forest Meteorol* **311**, 108681 (2021).
65. Harris, S. & Pedersen, D. Thermal regimes beneath coarse blocky materials. *Permafr. Periglac. Process.* **9**, 107–120 (1998).
66. Walvoord, M. A. & Kurylyk, B. L. Hydrologic impacts of thawing permafrost-a review. *Vadose Zone J.* **15**, 1–20 (2016).
67. Hartikainen, J. et al. *Evaluation of the permafrost models used in the SR-Site and SR-PSU safety assessments against Greenland GAP-site bedrock temperatures* (SKB, 2022).
68. Lewkowicz, A. G., Etzelmüller, B. & Smith, S. L. Characteristics of discontinuous permafrost based on ground temperature measurements and electrical resistivity tomography, Southern Yukon, Canada. *Permafr. Periglac. Process.* **22**, 320–342 (2011).
69. Muñoz-Sabater, J. et al. ERA5-Land: a state-of-the-art global reanalysis dataset for land applications. *Earth Syst. Sci. Data* **13**, 4349–4383 (2021).
70. Riseborough, D., Shiklomanov, N., Etzelmuller, B., Gruber, S. & Marchenko, S. Recent advances in permafrost modelling. *Permafr. Periglac. Process.* **19**, 137–156 (2008).
71. Weindorf, D. C. & Zhu, Y. Spatial Variability of Soil Properties at Capulin Volcano, New Mexico, USA: Implications for Sampling Strategy. *Pedosphere* **20**, 185–197 (2010).
72. Chen, T. & Guestrin, C. Multimodal classification of urban micro-events. In *Proc. 22nd ACM SIGKDD International Conference on Knowledge Discovery and Data Mining* 785–794 (Association for Computing Machinery, 2016).
73. Lundberg, S. M. & Lee, S.-I. A unified approach to interpreting model predictions. In *Proc. 31st International Conference on Neural Information Processing Systems* 4768–4777 (Curran Associates Inc., 2017).
74. Fyodorov-Davydov, D. et al. Ninth international conference on permafrost. In *Proc. 9th International Conference on Permafrost* 481–486 (Institute of Northern Engineering, USA).
75. Oblogov, G. E. et al. Methane content and emission in the permafrost landscapes of Western Yamal, Russian Arctic. *Geosciences* **10**, 412 (2020).
76. Langer, M., Westermann, S., Heikenfeld, M., Dorn, W. & Boike, J. Satellite-based modeling of permafrost temperatures in a tundra lowland landscape. *Remote Sens. Environ.* **135**, 12–24 (2013).
77. Varlamov, S. P., Skachkov, Y. B. & Skryabin, P. N. Long-term variability in ground thermal state in central Yakutia’s Tuymaada Valley. *Land* **10**, 1231 (2021).
78. French, H. M. Periglacial involutions and mass displacement structures, Banks Island, Canada. *Geografiska Annaler Ser. A Phys. Geogr.* **68**, 167–174 (1986).
79. Ednie, M. & Smith, S. L. *Establishment of community-based permafrost monitoring sites and initial ground thermal data, Baffin region, Nunavut*. (Geological Survey of Canada= Commission géologique du Canada, 2011).
80. Romanovsky, V., Cable, W., Walker, D., Yoshikawa, K. & Marchenko, S. Last decade of changes in ground temperature and active layer thickness in the high canadian arctic and in barrow. *AGU Fall Meet. Abstr.* **2013**, B31H–06 (2013).
81. Farquharson, L. M. et al. Climate change drives widespread and rapid thermokarst development in very cold permafrost in the Canadian High Arctic. *Geophys. Res. Lett.* **46**, 6681–6689 (2019).
82. Christiansen, H. H. et al. The thermal state of permafrost in the Nordic area during the International Polar Year 2007–2009. *Permafr. Periglac. Process.* **21**, 156–181 (2010).
83. Strand, S. M., Christiansen, H. H. & Gilbert, G. L. Permafrost thermal dynamics and cryostratigraphy at Villum Research Station, Station Nord, Eastern North Greenland (81° N). *J. Geophys. Res. Earth Surf.* **127**, e2021JF006502 (2022).
84. Westermann, S. et al. Future permafrost conditions along environmental gradients in Zackenberg, Greenland. *Cryosphere* **9**, 719–735 (2015).
85. Ødegård, R. S., Isaksen, K., Eiken, T. & Sollid, J. L. MAGST in mountain permafrost, Dovrefjell, southern Norway, 2001–2006. *Int. Conf. Permafr. Univ. Alsk. Fairbanks* **29**, 1311–1315 (2008).
86. Stenman, V. Quantifying palsa degradation dynamics using UAV imagery. *Umea University*, *Umea*, *Sweden* 1–27 (2024).
87. Fu, Z.-T., Wu, Q.-B., Wang, L.-Y. & Liu, Y.-L. Response of soil hydrothermal processes within the active layer to variable alpine vegetation conditions on the Qinghai-Tibet Plateau. *Adv. Clim. Change Res.* **14**, 200–212 (2023).

88. Lin, Z. et al. High spatial density ground thermal measurements in a warming permafrost region, Beiluhe Basin, Qinghai-Tibet Plateau. *Geomorphology* **340**, 1–14 (2019).
89. Jin, H. J., Yu, Q. H., Wang, S. L. & Lü, L. Z. Changes in permafrost environments along the Qinghai–Tibet engineering corridor induced by anthropogenic activities and climate warming. *Cold Reg. Sci. Technol.* **53**, 317–333 (2008).
90. Wu, J., Sheng, Y., Wu, Q. & Wen, Z. Processes and modes of permafrost degradation on the Qinghai-Tibet Plateau. *Sci. China Earth Sci.* **53**, 150–158 (2010).
91. Wang, Q. et al. Hydro-thermal processes and thermal offsets of peat soils in the active layer in an alpine permafrost region, NE Qinghai-Tibet plateau. *Glob. Planet. Change* **156**, 1–12 (2017).
92. Hrbacek, F. & Uxa, T. The evolution of a near-surface ground thermal regime and modeled active-layer thickness on James Ross Island, Eastern Antarctic Peninsula, in 2006–2016. *Permafr. Periglac. Process.* **31**, 141–155 (2019).
93. Hrbacek, F., Nývlt, D. & Láska, K. Active layer thermal dynamics at two lithologically different sites on James Ross Island, Eastern Antarctic Peninsula. *CATENA* **149**, 92–602 (2016).
94. Kňažková, M., Hrbacek, F., Kavan, J. & Nývlt, D. Effect of hyaloclastite breccia boulders on meso-scale periglacial-aeolian landsystem in semi-arid Antarctic environment, James Ross Island, Antarctic Peninsula. *Cuad. Investig. Geogr.* **46**, 7–31 (2020).
95. Ramos, M. et al. Recent shallowing of the thaw depth at Crater Lake, Deception Island, Antarctica (2006–2014). *Catena* **149**, 519–528 (2017).
96. Schaefer, C. et al. Penguin activity modify the thermal regime of active layer in Antarctica: a case study from Hope Bay. *CATENA* **149**, 582–591 (2017).
97. Hrbacek, F. et al. Effect of climate and moss vegetation on ground surface temperature and the active layer among different biogeographical regions in Antarctica. *CATENA* **190**, 104562 (2020).
98. Hrbáček, F. et al. Permafrost and active layer research on James Ross Island: an overview. *Czech Polar Rep.* **9**, 20–36 (2019).
99. De Pablo, M., Ramos, M. & Molina, A. Thermal characterization of the active layer at the Limnopolar Lake CALM-S site on Byers Peninsula (Livingston Island), Antarctica. *Solid Earth* **5**, 721–739 (2014).
100. Almeida, I. C. et al. Long term active layer monitoring at a warm-based glacier front from maritime Antarctica. *CATENA* **149**, 572–581 (2017).
101. Rudolph, E., Meiklejohn, I., Hansen, C., Hedding, D. & Nel, W. Rock glaciers in the Jutulsessen, Dronning Maud Land, East Antarctica. *Pol. Polar Res.* **39**, 1–17 (2018).
102. Lin, Z., Burn, C., Niu, F., Luo, J., Liu, M. & Yin, G. The thermal regime, including a reversed thermal offset, of arid permafrost sites with variations in vegetation cover density, Wudaoliang Basin, Qinghai-Tibet Plateau. *Permafr. Periglac. Process.* **26**, 142–159 (2015).

Acknowledgements

This study was supported by the National Natural Science Foundation of China (42571181), Western Young Scholars project of the Chinese Academy of Sciences of China (D. Luo), and the Science and Technology program of Gansu Province (Grant No. 23ZDFA017) and Longyuan Young Talents (D. Luo).

Author contributions

J.L. and D.L. conceived the idea and methodology. J.L. performed the primary data analysis, visualization, and wrote the main manuscript text. D.L. acted as corresponding author, supervised the project, and contributed significantly to the writing and editing. Q.W., W.D., H.J., and O.M. provided regional data expertise, contributed to the interpretation of results. F.C., S.L., and R.D.Ş. contributed to data processing and manuscript refinement. All authors reviewed the manuscript.

Competing interests

The authors declare no competing interests.

Additional information

Supplementary information The online version contains supplementary material available at https://doi.org/10.1038/s41612-025-01235-1.

Correspondence and requests for materials should be addressed to Dongliang Luo.

Reprints and permissions information is available at http://www.nature.com/reprints